HHS Public Access

Author manuscript

*Mol Cell*. Author manuscript; available in PMC 2020 February 21.

Published in final edited form as:

*Mol Cell*. 2019 February 21; 73(4): 763–774.e10. doi:10.1016/j.molcel.2018.11.033.

# An isoprene lipid binding protein promotes eukaryotic coenzyme Q biosynthesis

**Danielle C. Lohman**[#1,2], **Deniz Aydin**[#3], **Helaina C. Von Bank**[1], **Robert W. Smith**[2], **Vanessa Linke**[4], **Erin Weisenhorn**[5], **Molly T. McDevitt**[2], **Paul Hutchins**[4,6], **Emily M. Wilkerson**[4], **Benjamin Wancewicz**[4], **Jason Russell**[1,6], **Matthew S. Stefely**[1,2], **Emily T. Beebe**[2], **Adam Jochem**[1], **Joshua J. Coon**[1,4,5,6], **Craig A. Bingman**[1,2], **Matteo Dal Peraro**[3,7,*], and **David J. Pagliarini**[1,2,7,8,*]

[1]Morgridge Institute for Research, Madison, WI 53715, USA. [2]Department of Biochemistry, University of Wisconsin–Madison, Madison, WI 53715, USA. [3]Institute of Bioengineering, School of Life Sciences, École Polytechnique Fédérale de Lausanne (EPFL), 1015 Lausanne, Switzerland. [4]Department of Chemistry, University of Wisconsin–Madison, Madison, WI 53715, USA. [5]Department of Biomolecular Chemistry, University of Wisconsin–Madison, Madison, WI 53715, USA. [6]Genome Center of Wisconsin, Madison, WI 53715, USA. [7]Senior author. [8]Lead Contact

[#] These authors contributed equally to this work.

## SUMMARY

The biosynthesis of coenzyme Q presents a paradigm for how cells surmount hydrophobic barriers in lipid biology. In eukaryotes, CoQ precursors—among nature's most hydrophobic molecules—must somehow be presented to a series of enzymes peripherally associated with the mitochondrial inner membrane. Here, we reveal that this process relies on custom lipid-binding properties of COQ9. We show that COQ9 repurposes the bacterial TetR fold to bind aromatic isoprenes with high specificity, including CoQ intermediates that likely reside entirely within the bilayer. We

[*]Correspondence should be addressed to D.J.P. (dpagliarini@morgridge.org) or M.D.P (matteo.dalperaro@epfl.ch).

AUTHOR CONTRIBUTIONS

D.C.L., D.A., M.D.P., and D.J.P conceived of the project and its design and wrote the manuscript. D.C.L., H.C.V., R.S., M.S.S., E.T.B., and A.J. prepared samples and performed biochemical experiments. D.A. performed computational experiments and C.B. solved the crystal structures. V.L., E.W., M.T.M., P.H., and E.W. acquired mass spectrometry data. D.C.L., D.A., E.T.B., C.B., P.J., J.R., J.J.C., M.D.P., and D.J.P. analyzed data.



ACCESSION CODES

The atomic coordinates and structure factors have been deposited in the Protein Data Bank, www.pdb.org (PDB ID codes 6AWL, 6DEW).

DECLARATION OF INTERESTS

J.J.C. is a consultant for Thermo Fisher Scientific.

DATA AND SOFTWARE AVAILABILITY

Datasets for mass spectrometry data: Spreadsheet S2.

The crystallography coordinates have been deposited in the Protein Data Bank under ID codes 6AWL and 6DEW.

Raw image data has been deposited in Mendeley: http://dx.doi.org/10.17632/63ztbyhx5h.1

Raw mass spectrometry files have been deposited in Chorus under accession numbers 1532 (proteomics) and 1533 (lipidomics).

reveal a process by which COQ9 associates with cardiolipin-rich membranes and warps the membrane surface to access this cargo. Finally, we identify a molecular interface between COQ9 and the hydroxylase COQ7, motivating a model whereby COQ9 presents intermediates directly to CoQ enzymes. Overall, our results provide a mechanism for how a lipid binding protein might access, select, and deliver specific cargo from a membrane to promote biosynthesis.

## Graphical Abstract:

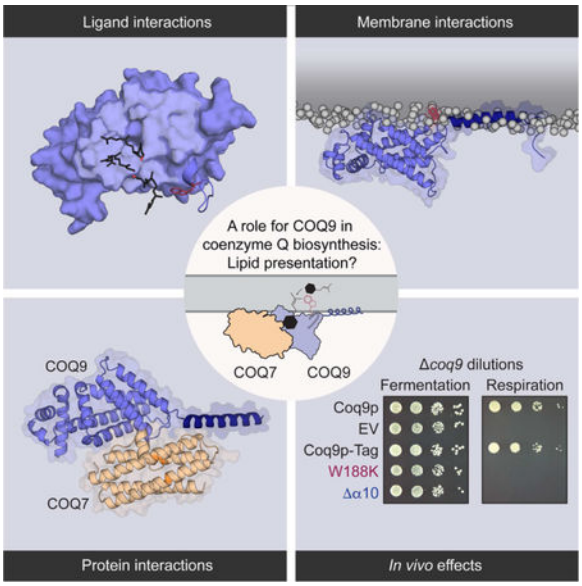


## eTOC BLURB

Lipid metabolism and transport relies on proteins that operate at the membrane-water barrier and have dynamic interactions with membranes, lipids, and other proteins. Lohman et al. report mechanistic insights into how COQ9 might access, select, and present specific membrane-cargo to a peripheral membrane enzyme during coenzyme Q biosynthesis.

### Keywords

Coenzyme Q; lipid-binding protein; peripheral membrane protein; mitochondria

## INTRODUCTION

The synthesis and transport of biological lipids in a largely aqueous cellular terrain poses a longstanding problem in biology (van Meer et al., 2008) (Prinz, 2010). A requisite first step in these processes is to access and separate a lipid from its local membrane environment. One of nature's strategies for dealing with such hydrophobicity challenges is to employ lipid binding proteins, which possess diverse modes-of-action. Transmembrane enzymes, like stearoyl-CoA desaturase, penetrate biological membranes and bring enzymatic function to the hydrophobic milieu (Bai et al., 2015). Lipid chaperones, like acyl carrier protein (Chan and Vogel, 2010) (Crosby and Crump, 2012) or Ups1/Mdm35 (Connerth et al., 2012) (Watanabe et al., 2015; Yu et al., 2015), solubilize lipids in a hydrophobic pocket and

transport them to soluble enzymes or insert them into membranes. Lipid liftases, like saposin C (Rossmann et al., 2008) or PlsC (Robertson et al., 2017) act at the membrane-water barrier to partially lift the lipid from the bilayer. Biosynthesis and spatiotemporal distribution of cellular lipids, from fatty acids to sterols, may depend on one or more of these strategies.

Coenzyme Q is a redox-active isoprene lipid that serves as a cofactor for numerous enzymes across all domains of life (Stefely and Pagliarini, 2017). Deficiency in CoQ is linked to many rare inborn errors of metabolism, and to common diseases including Parkinson's and type II diabetes mellitus (Fazakerley et al., 2018; Hughes et al., 2017; Stefely and Pagliarini, 2017). The molecular structure of CoQ is remarkable: its extraordinary isoprene tail—composed of 50 carbons in humans—places it among the most hydrophobic molecules in nature. This hydrophobicity keeps CoQ sequestered within the inner leaflet of the inner mitochondrial membrane where it passes electrons between complexes I & II and complex III in the electron transport chain. The CoQ tail is attached to an immature head group precursor at an early step in CoQ biosynthesis. In eukaryotes, enzymes within complex Q (a.k.a., the CoQ synthome) then modify this precursor to generate mature CoQ (Figure S1A) (Stefely and Pagliarini, 2017; Tran and Clarke, 2007). For these modifications to occur, complex Q enzymes must gain access to these hydrophobic precursors, which, like mature CoQ (Metz et al., 1995; Ulrich et al., 1985), are thought to reside within the hydrophobic portion of the membrane (Stefely and Pagliarini, 2017); however, how this access is granted remains unknown.

Recently, we revealed that COQ9—a poorly characterized protein associated with CoQ biosynthesis that structurally resembles the TetR family (TFR) of proteins (Lohman et al., 2014)—can bind lipids, suggesting that it may help complex Q overcome this hydrophobic challenge. Loss of COQ9 function in many organisms results in severe CoQ deficiency and underlies human disease, demonstrating its central role in this pathway (Danhauser et al., 2016; Duncan et al., 2009; Garcia-Corzo et al., 2013; Johnson et al., 2005; Luna-Sanchez et al., 2015; Smith et al., 2018). However, which lipid(s) COQ9 binds, how it accesses this cargo, and how this binding may assist other pathway enzymes have remained open questions.

Here, we investigate the molecular mechanism of COQ9 lipid-binding biochemically and computationally. We find that COQ9 binds aromatic isoprene lipids, accesses membranes via a terminal amphipathic helix, and that both of these functions are crucial to its biological role in CoQ production. We further establish a likely molecular interface between COQ9 and COQ7—the hydroxylase that catalyzes the penultimate step in CoQ biosynthesis. Collectively, these data suggest models in which COQ9 enables CoQ biosynthesis by accessing CoQ intermediates from the leaflet of the mitochondrial inner membrane and presenting them to a biosynthetic enzyme in the pathway.

## RESULTS

### COQ9 specifically binds aromatic isoprenes

We recently reported the fortuitous co-crystallization of COQ9 with a mixture of phospholipids (Lohman et al., 2014). This discovery, along with structural homology to

ligand binding domains of the TFRs and a predominantly hydrophobic cavity, defined COQ9 as a lipid-binding protein. Yet, the identity of *bona fide* COQ9 ligands remains unknown.

To identify endogenous lipid ligands of COQ9, we purified a tagged version of its yeast ortholog (Coq9p-FLAG) from *Saccharomyces cerevisiae* and identified ligands by mass spectrometry. Among various co-purifying lipids were several CoQ intermediates (Figure S1C,S1D; Spreadsheet S2). Membrane-associated proteins purified from endogenous sources are often accompanied by non-specific lipids. Therefore, to distinguish specific lipid interactions from non-specific binders, we mutated the highly conserved, surface-exposed tryptophan that resides near the co-crystallizing phospholipid in our previous COQ9 structure (Figure S1E) and is essential for COQ9 function (Lohman et al., 2014). Interestingly, this mutation was not well tolerated in *S. cerevisiae* (see Figure 6), so we performed these experiments in *Escherichia coli*, which lack a COQ9 homolog.

Specifically, we purified tagged (His-MBP) versions of human $COQ9^{N\Delta79}$ (the version of COQ9 whose structure we solved previously; see Table S1), $COQ9^{N\Delta79,W240K}$ (this same construct with the tryptophan mutated to lysine), and His-MBP alone from *E. coli*, and again identified co-purifying lipids by mass spectrometry (Figure 1A, Spreadsheet S2). Consistent with our previous work, phospholipids were the most abundant species co-purifying with COQ9 (Lohman et al., 2014); however, the W240K construct also co-purified with many phospholipids (Figure 1A). Remarkably, all identified lipids specifically enriched in WT $COQ9^{N\Delta79}$ were aromatic isoprenes, including $CoQ_{(reduced)}$, menaquinone (a bacteria-specific CoQ-like molecule), and their various precursors (Figure 1B,S1F). This enrichment in lipids resembling CoQ was not due to a global change in lipid levels in the *E. coli* expressing the recombinant protein (Figure S1G).

To understand how COQ9 accommodates isoprenes, we co-crystallized COQ9 with the isoprene lipid geranylgeraniol (Figure 1C), as CoQ intermediates themselves have low solubility and are not commercially available. We performed these co-crystallization experiments with a truncated protein ($COQ9^{N\Delta79,C\Delta31}$) to remove a C-terminal amphipathic helix that previously co-crystallized near the lipid binding site, possibly occluding ligand entry into the binding pocket when COQ9 is not associated with a membrane (Figure S2E). We determined the geranylgeraniol:$COQ9^{N\Delta79,C\Delta31}$ structure to 2 Å (Table 1, PDB: 6DEW). Six isoprene positions on multiple COQ9 chains in the unit cell were well-defined in the electron density (Figure S2A,S2B), with isoprenes commonly positioned along a hydrophobic surface of COQ9 and in the hydrophobic cavity (Figure 1C,S2C). Additionally, the α7-α8 loop that contains W240 adopted multiple conformations in the crystal lattice, moving up to 17.7 Å, indicating dynamic movement of the residue that conferred ligand specificity above (Figure S2D). The multiple isoprene positions suggest a model whereby the long-chain isoprene of a CoQ-like molecule would occupy the hydrophobic regions of COQ9 while the aromatic head group extends towards a flexible W240 (Figure 1D). Together, the co-purification of COQ9 with CoQ intermediates from an endogenous context in yeast, its selective co-purification with several aromatic isoprenes from bacteria, and its crystallization with an isoprene lipid suggest that binding CoQ isoprene intermediate(s) is central to COQ9's molecular function. To our knowledge, this is the first lipid binding protein with specificity for this lipid class.

### The amphipathic 10th α-helix of COQ9 drives membrane association

Within mitochondria, CoQ isoprene intermediates are thought to be either embedded in the inner mitochondrial membrane (IMM), like mature CoQ, or to be channeled through the membrane-associated complex Q in a 'metabolon'-like fashion (Stefely and Pagliarini, 2017). We sought to define how COQ9 might access CoQ intermediates from the IMM and how COQ9 accessed the membrane-embedded lipids reported here (Figure 1). In addition to its core TetR fold—a base architecture that can enable binding of specific metabolites, including hydrophobic polyketides and fatty acids (Cuthbertson and Nodwell, 2013; Ramos et al., 2005; Yu et al., 2010a)—COQ9 also possesses a distinct, amphipathic C-terminal 10th α-helix (α10) not typical among TFR proteins (Figure 2A,2B). Similar structural features are used by other lipid binding proteins to drive their interactions with membranes (Chua et al., 2017; Cornell, 2016; Suetsugu et al., 2014), leading us to hypothesize that α10 has a role outside the canonical TetR fold, potentially to localize COQ9 to membrane-bound cargo in the IMM. We determined the structure of the α10-containing $COQ9^{N\Delta 79}$ to 2 Å resolution and discovered that α10 extends away from the rest of COQ9, forming a crystal contact at the interface of two adjacent COQ9 chains in the crystal lattice (Figure S2F; Table 1, PDB: 6AWL). Furthermore, coarse-grained molecular dynamics (CG-MD) simulations of COQ9 in solution revealed a dynamic 200-degree movement of α10 where α10 collapsed on the hydrophobic surface of COQ9 within 3 μs, moved across this surface for 7 μs, and eventually re-extended (Figure 2C, Movie S1).

To examine the mechanism of COQ9 membrane association, including a potential role for α10, we performed CG-MD simulations of COQ9 with membrane models comprised of phosphatidylcholine (PC), phosphatidylethanolamine (PE), and cardiolipin (CL) to resemble the IMM (Daum, 1985). In these simulations, COQ9 invariably associated with the membrane in a multi-step fashion (Figure 3A, Movie S2). COQ9 first diffused in the aqueous environment until two lysines (K288, K291 in Step 1) in the α9-α10 loop interacted electrostatically with phosphate head groups of negatively charged cardiolipin. Second, hydrophobic residues of α10 (V290, L297, V298, L301, M302 in Step 2) interacted with the membrane, reaching the glycerol backbones of membrane phospholipids. Next, the protein core (α1-α9) approached the membrane, first with α8 (W240, Y241 in Step 3) and then with α7 (P210, H211 in Step 4). Finally, residues along the hydrophobic surface of COQ9 were exposed to the membrane (P201, L204, I206, M208, L209, I213, L217, L256 in Step 5).

To investigate the step-wise membrane binding mechanism biochemically, we tested whether COQ9 alanine mutants of residues contributing to Steps 1–4 affected liposome co-flotation (Figure 3A,3B,3C,S3A). Consistent with simulations, neutralizing the electrostatic interaction in Step 1 decreased membrane association, while mutations to residues mediating Steps 3 and 4 did not (Figure 3B,3C). Alanine mutants of α10 hydrophobic residues in Step 2 reduced liposome association the most (Figure 3B,3C). Similarly, mutating α10 hydrophobic residues to serine or fully deleting α10 reduced liposome association by more than 60% (Figure 3D,3E). Importantly, all tested mutants had robust thermal melt curves, indicating stably folded protein (Figure S3B).

## COQ9 association with cardiolipin-rich membranes warps the lipid bilayer

COQ9 membrane association was strongly influenced by CL, a quintessential mitochondrial lipid with key roles in cristae organization and respiratory supercomplex formation (Acehan et al., 2011; Gohil et al., 2004; Ikon and Ryan, 2017; Zhang et al., 2005). In CG-MD simulations featuring a simple PC-based membrane model, COQ9, although approaching the membrane several times, was not able to establish a specific and stable interaction with the membrane (Figure 4A,S3G). Consistently, cardiolipin specificity was observed biochemically in liposome co-flotation assays (Figure 4B,4C,S3C–S3F).

Our simulations also revealed striking features of membrane lipid organization upon COQ9 association. In Step 5, the hydrophobic surface of COQ9 displaced lipid head groups, creating a deformation in the membrane, an area void of phosphate head groups, and a higher concentration of CL surrounding α7, α8 and α10 (Figure 4D, Movie S3). Lipids interacting with COQ9 had low diffusion coefficients, where recurrently binding CL molecules persisted for over 5 μs and established favorable interactions with residues K288 and W240 (Figure S3H). The local deformation of the membrane surface caused lipids surrounding COQ9 to be orthogonally displaced from the membrane surface by ~5 Å while their hydrophobic tails entered the hydrophobic cavity of COQ9 (Figure 4E,S3I, Movie S4). Such lifting of lipids off the membrane by a peripheral membrane protein is reminiscent of, although distinct from, the mechanism observed in a previous MD study reporting the partial extraction of a single PC molecule into the hydrophobic pocket of phosphatidylinositol transfer protein-α (PITPα) (Grabon et al., 2017). These observations in CG-MD simulations provide a potential molecular mechanism for how COQ9 extracted lipid cargo in the adventitious co-crystallization with phospholipids and in the specific co-purification with aromatic isoprenes. Collectively, our computational and biochemical findings support a model whereby the amphipathic α10 drives membrane association in a multi-step fashion and poises the hydrophobic surface of COQ9 to deform the IMM in order to access membrane-bound lipids.

## COQ9 interaction and interface with COQ7 suggest a lipid presentation role

Prior studies in human patients (Danhauser et al., 2016; Duncan et al., 2009; Smith et al., 2018), mice (Garcia-Corzo et al., 2013; Lohman et al., 2014; Luna-Sanchez et al., 2015; Wang et al., 2017), and yeast (He et al., 2015; Hsieh et al., 2007; Johnson et al., 2005) have suggested that COQ9 may be especially important for the C6-hydroxylation step of CoQ biosynthesis performed by the di-iron carboxylate hydroxylase COQ7 (Behan and Lippard, 2010; Lu et al., 2013; Stenmark et al., 2001b; Tran et al., 2006). Previously, we identified an *in vitro* interaction between COQ9 and COQ7, revealing through mutagenesis that a conserved surface patch of COQ9 (D237, W240, Y241 in the flexible α7-α8 loop, Figure S2D) mediates COQ7 binding (Lohman et al., 2014). Here, we identified residues of COQ7 that, reciprocally, are required for COQ9 binding (Figure 5A,5B,S4A). We designed 13 COQ7 point mutants based on evolutionary conservation and predicted solvent accessibility, and we discovered that mutants within a predicted loop of COQ7 and mutants at the C-terminus fail to bind COQ9 (Figure 5A,5B,S4B). Interestingly, some of these residues, although generally conserved, are absent in certain nematodes that lack COQ9 homologs (Figure S4C).

We used these biochemical data reporting on possible COQ9-COQ7 intermolecular contacts combined with the orientation of COQ7 and COQ9 on the IMM identified by our individual simulations (Figure S5A) to determine a potential molecular interface of the complex. The modeled conformation that fulfills these spatial constraints places the COQ9 hydrophobic surface (where isoprenes bind) adjacent to the COQ7 active site (Figure 5C,5D). The protein-protein interface comprises α7, α8, and the α7-α8 loop of COQ9 with α1, α2, and a loop of COQ7, where key contacting interfacial residues include W240 and Y241 of COQ9, and P108 and W115 of COQ7.

To visualize this complex in a more endogenous context, we incorporated a partial COQ7 substrate (demethoxy CoQ with 5 isoprene units, $DMQ_5$) into our COQ9 model associated with the IMM (Figure 5C,5D,5E) (Hsieh et al., 2007; Tran and Clarke, 2007). In this conformation, molecular docking predicted that two isoprene units of $DMQ_5$ fit into the COQ9 hydrophobic cavity in a pose consistent with a co-crystallized isoprene (RMSD=1.5 Å, Figure 1C,S5B). The rest of the $DMQ_5$ tail lay on the hydrophobic surface such that the aromatic head group extends towards W240—the residue that conferred aromatic isoprene binding specificity above (see Figure 1) (Figure 5C,5E,S5B,S5C). The predicted architecture of the membrane-bound COQ9-COQ7 complex suggests that COQ9 could lift the COQ7 substrate from the membrane and present it to the COQ7 active site, similar to lipid metabolic nanoreactors (Bankaitis et al., 2010; Ile et al., 2006). Moreover, we again observed in simulations an increased CL occupancy around COQ7 (Figure S5D), as was observed for COQ9 simulations (Figure 4D), suggesting that this lipid species can be important for mediating the interaction of these proteins with the IMM and thus facilitating COQ9-COQ7 complex formation.

### COQ9 lipid- and membrane-binding residues are critical for CoQ production *in vivo*

The work above identifies structural features of COQ9 predicted to facilitate CoQ intermediate selection from the IMM and delivery to COQ7. To test the importance of these features *in vivo,* we engineered two Coq9p-FLAG mutants in *S. cerevisiae*: W188K (analogous to W240K in humans, to disrupt aromatic isoprene and COQ7 binding) and Δα10 (to disrupt membrane binding) (Figure 6A). Both mutants failed to rescue respiratory growth in Δ*coq9 S. cerevisiae* (Figure 6B,S6A), indicating their importance for core COQ9 function (Lohman et al., 2014). Additionally, Coq9p chimeras possessing other amphipathic or transmembrane domains in lieu of its α10 could not rescue Δ*coq9* respiratory growth defects (Figure S7A-D).

Previous work has shown that certain defects in CoQ biosynthesis can be bypassed by providing modified CoQ precursors that obviate the need for a specific enzyme (Luna-Sanchez et al., 2015; Pierrel, 2017; Wang et al., 2017) (Figure S1B), or by overexpressing Coq8p (He et al., 2014; Xie et al., 2012), which confers stability to complex Q by an unclear mechanism. Overexpression of Coq8p-FLAG partially rescued Δ*coq9* yeast expressing W188K, but had no effect on Δα10, consistent with these mutants disrupting CoQ biosynthesis through distinct means (i.e., isoprene binding and membrane binding, respectively) (Figure 6C,S6B). Additionally, levels of the Coq7p substrate (DMQ) were particularly elevated in the Coq8p-FLAG + $Coq9p^{W188K}$ strain (Figure S6D), and 2,4-

dihydroxybenzoate—a compound capable of specifically bypassing a Coq7p enzymatic defect—augmented the Coq8p-FLAG rescue of the W188K growth defect. Together, these results clearly indicate compromised Coq7p activity in this strain, as would be predicted from our experiments above. Notably, both strains contained CoQ intermediates that resembled those in Δ*coq9* + Coq8p-FLAG (including those associated with Coq6p defects, Figure S6D) (He et al., 2015; Ozeir et al., 2015; Xie et al., 2012), which indicates Coq9p is important for other biosynthesis steps, possibly through a role in complex Q formation or stabilization. Interestingly, both mutants inhibited respiratory growth in WT yeast, demonstrating that they are both non-functional and also confer dominant-negative inhibition (Figure 6D,S6C). Mass spectrometry-based lipidomics and proteomics analyses revealed that these strains had decreased levels of CoQ, enhanced levels of an early CoQ biosynthetic intermediate (PPAB), and decreased levels of complex Q proteins, consistent with the predicted disruption in CoQ biosynthesis (Figure 6D, 6E, 6F). Together, these *in vivo* data further support the functional importance of COQ9 isoprene-, membrane-, and COQ7-binding, and suggest a model whereby COQ9 acts as a 'lipid presenter' to overcome hydrophobic barriers associated with CoQ biosynthesis.

## DISCUSSION

The spatiotemporal organization of lipids in metabolism, signaling, and membrane structure poses significant biophysical barriers within the largely aqueous cellular environment. Many strategies—from lipid transport proteins (Wong et al., 2017) to organelle contact site complexes (Murley and Nunnari, 2016; Tamura and Endo, 2017) (Lahiri et al., 2015)—serve to minimize these barriers, and each begins with recognition of membrane-embedded cargo. CoQ biosynthesis, the bulk of which occurs within complex Q or the CoQ metabolon (a supramolecular complex of enzymes and structural elements (Srere, 1985)), shares these hydrophobic barriers. Several additional features make CoQ biosynthesis a notable case study in lipid biology: the discovery of a key lipid-binding protein, the tethering of complex Q to the inner mitochondrial membrane, the proposed dynamic nature of complex Q, and the exceptional hydrophobicity of CoQ intermediates (He et al., 2014; Stefely and Pagliarini, 2017; Tran and Clarke, 2007). We sought to further define the mechanism of COQ9 lipid binding and its role in enabling the CoQ biosynthetic process.

Recent advances in structural biology, bioinformatics, and *in vitro* biochemistry have equipped researchers with powerful tools to study how cells manage lipid metabolism and transport (Malinina et al., 2017; Tatsuta et al., 2014) (Wong et al., 2017). Yet, defining the biochemical mechanisms that control lipid cargo selection faces the substantial challenge of studying protein function at the membrane-water barrier. Here, we combined molecular dynamics simulations with traditional biochemical and structural approaches to describe the stepwise mechanism for cargo selection by COQ9. We discovered that COQ9 uses a distinct amphipathic helix connected to a foundational ligand binding domain to associate with membranes. In our molecular simulations, COQ9 deforms the membrane bilayer by extruding polar head groups at the protein-IMM interface. During the simulation, this warping effect of the membrane surface allows lipid tails to be drawn into the COQ9 hydrophobic cavity at sites consistent with isoprene moieties found in our co-crystallization experiments. The creation of such a peculiar environment in the membrane—a continuous

and tightly sealed hydrophobic region encompassing both the IMM and COQ9—could be key to solving the hydrophobicity problem of extracting CoQ intermediates from the membrane. This mode of action shares parallels with the “liftase” model proposed for how lipid transfer proteins (e.g. saposins (Alattia et al., 2006; Hill et al., 2018), GM2-AP (Furst and Sandhoff, 1992), and PlsC (Robertson et al., 2017) overcome the topological challenge of reaching substrates located inside the membrane. Upon membrane binding, these proteins are envisaged to improve lipid accessibility and processing through modifying membrane organization (e.g. lifting lipids out of the membrane, distorting and destabilizing the membrane). We showed here, for the case of COQ9, that molecular simulations and biochemical approaches can be used together to molecularly dissect the mechanism of membrane reshaping and lipid trafficking adopted by lipid binding proteins.

This proposed role for COQ9 to retrieve CoQ intermediates from the bilayer is supported by its binding specificity for aromatic isoprenes. This specificity is guided by a highly conserved and mobile tryptophan (W240 in human or W188 in yeast), and the proximity of this residue to $DMQ_5$ in molecular docking experiments suggests that π-π stacking interactions could contribute to substrate specificity, to dynamic sensing, and/or to lipid presentation and transfer (Figure 1D). Importantly, CoQ intermediates are thought to be protected from water—whether they are embedded in the lipid bilayer, channeled through complex Q, or passed along the periphery of the IMM by a lipid chaperone. Correspondingly, COQ9 could act as a lipid presenter at the membrane surface and/or between enzymes in complex Q.

Lipid-presenting proteins are notoriously challenging to characterize because of their dynamic nature, their dependence on other proteins, and their function at the membrane-water barrier. The case of Coq9p is further complicated by its concurrent role in complex Q stability, as dysfunctional CoQ proteins can cause the degradation of complex Q. Nonetheless, perturbations to Coq9p membrane (α10) and lipid binding (W188) residues severely disrupt *in vivo* CoQ biosynthesis by compromising the integrity of complex Q stability and by hindering Coq7p enzymatic activity. The specific connection between Coq9p function and Coq7p activity is reflected in patients with primary CoQ deficiency caused by mutations to COQ9 (Danhauser et al., 2016; Duncan et al., 2009). To date, six reports of COQ9 patient mutations result in decreased levels of COQ7 and the apparent accumulation of the COQ7 substrate, DMQ (Danhauser et al., 2016; Duncan et al., 2009; Smith et al., 2018). Interestingly, one of the two reported patient mutations in COQ7 (L111P) is a point mutant at the predicted COQ9:COQ7 molecular interface (Wang et al., 2017). Our predicted architecture of the membrane-bound COQ9-COQ7 complex suggests that COQ9 could lift the COQ7 substrate from the membrane and present it to the COQ7 active site—a model reminiscent of lipid metabolic nanoreactors (Bankaitis et al., 2010; Ile et al., 2006), but one which will require further experimentation and structural analyses to validate.

In addition to mechanistic insights into how a peripheral membrane protein can extract membrane-embedded cargo, our work introduces a potential mechanism for the spatial organization of membrane lipids and, possibly, for complex Q seeding. In both our simulations and liposome co-flotation studies, CL had a role in the binding and dynamics of

COQ9-membrane interactions. Indeed, we recently demonstrated that CL likewise enhances the membrane association and ATPase activity of COQ8, a second poorly characterized protein in the CoQ pathway (Reidenbach et al., 2018). If complex Q is localized to specific sites on the mitochondrial cristae, these findings suggest that its position and assembly could be influenced by local CL concentration. Cardiolipin is known to have a pivotal role for the formation and stability of several inner mitochondrial membrane protein complexes (Acehan et al., 2011; Gohil et al., 2004; Zhang et al., 2005). Cardiolipin occupancy and persistency around COQ9 and COQ7 observed in our membrane binding simulations suggests that CL is important for establishing and maintaining the specific interaction of these proteins with the IMM, and thus for facilitating COQ7-COQ9 complex formation. These observations suggest that cardiolipin-rich areas might template the membrane with a preferential surface pattern able to favor COQ9-COQ7 complex formation, as well as the recruitment of other members of complex Q. Further study of the localization, components, and connectivity of complex Q will inform these models.

Finally, there is speculation that complex Q is not a static metabolon, but that it might instead form upon substrate availability, and that CoQ or a pathway intermediate is part of the complex (Gonzalez-Mariscal et al., 2014; Tran and Clarke, 2007). Work from us and others suggest Coq8p could assist with sensing and delivering substrates based on its lipid interactions, ATPase activity, and apparent ability to stabilize complex Q (Reidenbach et al., 2018) (Stefely et al., 2016b; Stefely et al., 2015) (Xie et al., 2012). The structural homology of COQ9 with ligand-sensing transcription factors also makes COQ9 a plausible “sensor” candidate (Lohman et al., 2014). Here, we introduce the flexible α7-α8 and α9-α10 loops that guide ligand interactions, COQ7-binding, and membrane interactions as possible key features in metabolon formation and activity.

Overall, our analyses present COQ9 as a new model for how nature employs peripheral lipid binding proteins to surmount hydrophobic challenges. These insights into how a protein can access, bind, and present a hydrophobic ligand may also inform new strategies to treat lipid deficiency disorders that are recalcitrant to supplementation, including many CoQ-related diseases. Moreover, our integrative approach combining structural, biochemical, and computational studies was effective at providing sub-nanometer resolution of COQ9 function at the protein-membrane interface and may thus serve as a model for interrogating other lipid binding proteins or lipid metabolism or signaling pathways whose investigations present similar challenges.

## STAR METHODS TEXT

### CONTACT FOR REAGENT AND RESOURCE SHARING

Further information and requests for resources and reagents should be directed to and will be fulfilled by the Lead Contact, Dave Pagliarini (dpagliairini@morgridge.wisc.edu).

### EXPERIMENTAL MODEL AND SUBJECT DETAILS

*Saccharomyces cerevisiae* strains (WT and *Δcoq9*) were the haploid MATalpha BY4742 (his3Δ1 leu2Δ0 lys2Δ0 ura3Δ0) from the gene deletion consortium (Thermo #YSC1054).

*Escherichia coli* strains for protein overexpression were BL21[DE3]-RIPL from Agilent and for cloning applications, DH5α from NEB were used. Unless specified otherwise, *E. coli* were grown at 37 °C in LB media with antibiotics and *S. cerevisiae* were grown at 30 °C in drop-out minimal media.

## METHOD DETAILS

**DNA constructs and cloning—**Recombinant DNA sources are listed in the Key Resource Table and the primers used in this study are listed in Spreadsheet S1. Point mutants were generated by standard site-directed mutagenesis while insertions and deletions were generated by standard PIPE (Klock et al., 2008) cloning methods.

### Protein expression and purification

**COQ9$^{NΔ79}$ and COQ9$^{NΔ79, CΔ31}$ expression and purification:** $His_8$-MBP-tev-COQ9$^{NΔ79}$ and mutants were expressed in *E. coli* (BL21[DE3]-RIPL strain) by autoinduction as previously described (Lohman et al., 2014). Cells were isolated and resuspended in buffer A supplemented with 1 mg/mL Lysozyme (Sigma): 50 mM HEPES pH 7.5, 400 mM NaCl, 0.3 mM TCEP, 0.25 mM PMSF, and peptide protease inhibitors: 500 ng/mL leupeptin hemisulfate, pepstatin A, chymostatin, aprotinin, and antipain dihydrochloride at pH 7.2. Cells were lysed by sonication (4 °C), clarified by centrifugation (15,000× *g*, 30 min, 4 °C), and bound to cobalt IMAC resin (TALON, Clontech, 1 hr, 4 °C). Resin was washed wit h Buffer A and his-tagged protein was eluted with Buffer A supplemented with 100 mM imidazole. Eluted protein was concentrated (50-kDa MW-cutoff spin filter, Merck Millipore Ltd.) and exchanged into Storage Buffer (20 mM HEPES pH 7.5, 150 mM NaCl, 0.3 mM TCEP). For experiments with untagged protein, $His_8$-MBP-COQ9$^{NΔ79}$ was incubated with TEV protease (prepared in-house, 1:50 TEV/fusion protein, mass:mass using $\varepsilon_{280}$ = 102,130 $M^{-1}cm^{-1}$ and MW = 71.3 kDa, 2 hrs, 25 °C), then bound to cobalt IMAC resin (1 hr, 4 °C). Cleaved COQ9 $^{NΔ79}$ ($\varepsilon_{280}$ = 36,130 $M^{-1}cm^{-1}$, MW = 27.4 kDa) was collected, concentrated (10-kDa MW-cutoff spin filter), and exchanged into Storage Buffer. Protein was aliquoted, frozen in $N_{2(l)}$, and stored at −80 °C.

**SII-COQ9$^{NΔ45}$ and $His_6$-COQ7$^{NΔ38}$ expression and purification:** SII-COQ9$^{NΔ45}$ and $His_6$-COQ7$^{NΔ38}$ were expressed and purified in wheat germ extract (WEPRO2240, CellFree Sciences, Matsuyama, Japan) as previously described (Lohman et al., 2014). Transcription reactions (0.2 mg/mL DNA, 20 mM magnesium acetate, 2 mM spermidine trihydrochloride, 10 mM DTT, 80 mM HEPES-KOH pH 7.8, 4 mM each NTP pH 7.0, 1.6 U/μL SP6 RNA polymerase (Promega, Madison, WI), and 1 U/μL RNasin (Promega)) were incubated for 4 h at 37 °C. Single or mixed 1:1 COQ9:COQ7 transcription products were added to wheat germ extract in a dialysis cup reaction: 60 O.D. wheat germ extract, 24 mM HEPES-KOH, pH 7.8, 100 mM potassium acetate, 6.25 mM magnesium acetate, 0.4 mM spermidine trihydrochloride, 4 mM DTT, 1.2 mM ATP, 0.25 mM GTP, 16 mM creatine phosphate, 0.0005% sodium azide, 0.04 mg/mL creatine kinase, 0.3 mM each amino acid at pH 7.0, and 5 μL of RNA. Translation reactions were incubated (18 hr, 22 °C) in 32-fold excess dialysis buffer (without wheat germ extract, creatine kinase, or RNA). Duplicate translations were pooled and centrifuged (5 min, 20,000×g, 10 °C). Soluble protein was incubated with

StrepTactin resin, washed in 25 mM HEPES pH 7.8, 150 mM NaCl, 1 mM DTT using a 96-well filter plate (HTS Multiscreen, Millipore), and eluted with 2.5 mM desthiobiotin.

## Biochemical assays

**Differential scanning fluorimetry:** DSF was performed as previously described (Lohman et al., 2014). Reactions (20 μL) of protein (2 μM), SYPRO Orange dye (Invitrogen) (5X), NaCl (150 mM), HEPES (100 mM, pH 7.5) were prepared in Micro Amp Optical 96 (0.2 mL) Well Reaction Plates and sealed with Optical Adhesive Covers (Applied Biosystems). Fluorescence was measured (excitation filter ×1 470 ± 15 nm and emission filter m4 623 ± 14 nm) during heating (15 to 95 °C, 0.017 °C/s) in Applied Biosystems Qua ntStudio 6 Flex Real Time PCR System. $T_m$ values were calculated in Protein Thermal Shift software (Applied Biosystems).

**Western blot:** Western blots of yeast whole cell lysate ($4\times10^7$ cells) were probed with primary α-FLAG (Sigma-Aldrich F1804), secondary α-mouse IgG (RDye® 800CW), then visualized on a LI-COR imager.

**Liposome co-flotation assays:** Liposomes were made with the following lipids from Avanti Polar Lipids reference: PC(#840051C); NBD-PE(#810145C); PE(#850725C); CL(#710335C). Unless otherwise specified, liposome compositions were PC/PE/CL/NBD-PE 68.9/9/22/0.1 molar percent. Lipid films were prepared by drying well-mixed lipids in organic solvent first under $Ar_{(g)}$ then by vacuum chamber (25-30 inHg, 17 hrs, 20 °C). The lipid film was reconstituted in HBS buffer (20 mM HEPES pH 7.5, 150 mM NaCl) to 10 mM total lipids by incubation (30 min, 30-35 °C) followed by 3 freeze/thaw cycles in $N_{2(l)}$. Liposomes were extruded through 100 nM membranes (Avanti Polar Lipids, 11 passes, 30-35 °C ) and used within 4 hours of preparation.

Liposome co-flotation was adapted from Connerth *et al.* (Connerth et al., 2012). Liposomes (100 μL) were incubated with protein (50 μL) (10 min, 20 °C) and final reactions contained: 2.5 μM protein, 6.66 mM liposomes, 20 mM HEPES pH 7.5, 150 mM NaCl. Sucrose (2.72 M, 110 μL) was added to the protein liposome mixture and transferred (250 μL) to an ultracentrifuge tube (Beckman #343776). A sucrose gradient in HBS was layered: 1.15 M sucrose with reaction (250 μL), 0.86 M sucrose (300 μL), 0.29 M sucrose (250 μL), and 150 μL HBS. After centrifugation (240,000×*g*, 1 h, 4 °C, Sorvall MX 120 Plus Micro-ultracentrifuge), fractions were removed from top (450 μL) to bottom (450 μL). Liposome content was quantified by NBD-PE fluorescence (excitation: 460 nm, emission: 535 nm) to validate flotation. Proteins in each fraction were $CHCl_3$:MeOH precipitated, following a method adapted from Wessel and Flugge (Wessel and Flugge, 1984) with methanol (1800 μL) and chloroform (450 μL). After vortexing, water (1350 μL) was added and samples were vortexed and centrifuged (5 min, 4,000×*g*, 20 °C). The upper aqueous layer was discarded and methanol (1000 μL) was added to the protein disc. After mixing by inversion, samples were centrifuged (5 min, 20,000×*g*, 20 °C) and all liquid removed. The precipitated protein pellet was vacuum dried (25-30 inHg, 30 min, 20 °C), resuspended in denaturing loading buffer with 10 mM DTT, and analyzed by SDS-PAGE. Protein bands were quantified by densitometry on a LiCOR Odyessey CLx (700 nm) using Image Studio v5.2 software. Error

bars represent standard deviation of co-flotations performed in parallel (n=2 or 3) and Student's *t*-test was used to determine statistical significance assuming two tailed distributions and equal variance.

***S. cerevisiae* growth assays—**Δ*coq9* or WT *S. cerevisiae* (BY4742) were transformed as previously described with p416GPD (Ura selection) plasmids encoding Coq9p variants and grown on Ura drop-out synthetic media plates containing glucose (2%, w/v) (Gietz and Woods, 2002). Individual colonies were used to inoculate starter cultures, which were incubated (30 °C, ×18 h, 230 rpm). Serial dilutions of yeast ($10^4$, $10^3$, $10^2$, or 10 yeast cells) were dropped onto $Ura^-$ agar media plates containing either fermentation (2% glucose, w/v) or respiration (3% glycerol, w/v) media and incubated (30 °C, 2-4 days). To assay yeast gro wth in liquid media, yeast from a starter culture were swapped into selective synthetic media with in fermentation (2% glucose, w/v) or respiration (3% glycerol 0.1% glucose, w/v) media at an initial density of $5\times10^6$ cells/mL (Stefely et al., 2016a). The cultures were incubated in a sterile 96 well plate with an optical, breathable cover seal (1140 rpm) and optical density readings were obtained every 10 min. For co-overexpression experiments, yeast were co-transformed with p413GPD (His selection) plasmids encoding Coq8p-FLAG and subsequent plating and growth assays performed in $Ura^-His^-$ media. For small molecule bypass experiments, small molecules were added to 1 mM final concentration to the growth assay media: 2,4-dihydroxybenzoic acid (Coq7p bypass, Sigma D109401); 3,4-dihydroxybenzoic acid (Coq6p bypass, Sigma P5630); vanillic acid (Coq6p+Coq3p bypass, sigma H36001); 4-hydroxy-2-methylbenzoic acid (Coq5p bypass, Sigma 653160).

**Crystallography—**COQ9 was purified as described in "*$COQ9^{N\Delta79}$ and $COQ9^{N\Delta79,\ C\Delta31}$ expression and purification*" and then subjected to size exclusion chromatography on HiLoad 16/600 Superdex 75 pg (GE Healthcare) in Storage buffer (20 mM HEPES pH 7.5, 150 mM NaCl, 0.3 mM TCEP). Fractions containing COQ9, assessed by SDS-PAGE, were pooled to >10 mg/mL, concentrated with a MW-cutoff spin filter, frozen in $N_{2(l)}$, and stored at −80 °C.

$COQ9^{N\Delta79}$ was screened for crystallization using IndexHT (Hampton Research) and JCSG+ (Molecular Dimensions) screens and optimized using a TTP Labtech Mosquito crystallization robot using MRC SD-2 sitting drop plates. Crystals were imaged using a UVEX-P UV/Visible microscope. 200 nL protein at 4.89 mg/mL in 10 mM HEPES buffer at pH 7.5 and 100 mM NaCl was mixed with 200 nL crystallization reagent. Optimized crystals were obtained from a reservoir of 21% w/v PEG3350, 0.25 M Nacl, 0.1 M bistris, pH 6.5. The crystal was cryoprotected by soaking the crystal in reservoir solution supplemented to 35% w/v PEG3350. Diffraction data was collected at the Advanced Photon Source on GM/CA@APS 23-ID-B beamline, using an Eiger 16M detector. Data was collected at 12keV (1.0332Å) 350 mm 0.2 degrees per frame, 0.2 seconds per frame, 70×50 micron slits, 40× attenuation. Data was reduced using XDS, scaled with XSCALE (Kabsch, 2010). The structure was solved by molecular replacement with Phaser in the Phenix suite (Adams et al., 2010) using PDB 4RHP as a search model (McCoy et al., 2007). The structure was refined using alternating rounds phenix.refine (Afonine et al., 2012) and model building in Coot (Emsley et al., 2010).

$COQ9^{N\Delta79,\ C\Delta31}$ was screened for crystallization using the same workflow as $COQ9^{N\Delta79}$. Reasonable crystals were obtained from ammonium sulfate and tris buffer. This crystallization condition was favored for isoprene co-crystallization trials, since polymeric precipitants like polyethylene glycol might be mistaken for isoprene alcohols. Initial optimization experiments using farnesol and geranylgeraniol in plastic crystallization plates yielded no obvious electron density for bound isoprenols. Optimal crystals were obtained by microseeding into droplets hanging from glass coverslips, hanging over glass concavity plates, sealed with perfluoroether oil. The reservoir solution was 50 microliters of 1.2 M ammonium sulfate, 0.1 M Tris buffer, pH 8.5, mixed with 4 microliters of neat geranylgeraniol, the majority of which formed a second phase. Two microliters of protein at 5.8 mg/mL, diluted from a 21.7 mg/mL protein stock in 160 mM NaCl, 20 mM HEPES buffer, pH 7.5 and 0.3 mM TCEP was mixed with 1 microliter of seed stock derived from a previous batch crystallization experiment conducted at 1.5 M ammonium sulfate, 0.1 M Tris pH 8.5. Crystals grew over a week. They were cryoprotected by supplementing the droplet with 2 microliters of reservoir solution, and then replacing it with 3 M ammonium sulfate, 0.1 M Tris pH 8.5, supplemented with neat geranylgeraniol. The droplet was allowed to equilibrate overnight, and crystals were harvested by drawing them through a layer of perfluoroether oil in a Mitegen microcrystal mount, wicking away excess mother liquor, and plunging then into liquid nitrogen. Data was collected at the Advanced Photon Source on LS-CAT 21-ID-D beamline, using a Eiger 9M detector. Data was collected at 100K, using an 11 keV (1.12723Å) beam, 170 mm, 0.2 degrees per frame, 50 micron beam. Data reduction, structure solution and refinement used the same workflow as $COQ9^{N\Delta79}$, except that a version of 6AWL with the $10^{th}$ helix truncated was used as the starting model for molecular replacement. Long tubes of electron density were observed at consistent sites on all of the monomers. Using constituents present in the crystallization mixture, the extent and shape of these features could only be successfully modeled using isoprenols. Features at these sites were less clear or absent in previous electron density maps from preceding crystallization attempts with isoprenols conducted in plastic 96 well plates. Isoprenols were docked into the electron density using phenix.ligandfit using geranylgeraniol, farnesol and geraniol as probes. Three farnesol (three isoprene units) and three geraniol (2 isoprene units) were successfully modeled into the most orderly sites.

## Molecular dynamics simulations

**Coarse-grained molecular dynamics simulations:** Coarse-grained molecular dynamics (CG-MD) simulations were used to investigate: (i) the interaction of COQ9 and COQ7 with bilayers containing different lipid compositions, (ii) the flexibility of the α9-α10 hinge allowing different structural placements of α10. All simulations were performed using the GROMACS (Van der Spoel et al., 2005) simulation package version 5.1.2 (Abraham et al., 2015). The systems were described with the MARTINI CG force field, together with the ElNeDyn (Elastic Network in Dynamics) approach to maintain the secondary structure of the protein (Marrink et al., 2007; Periole et al., 2009). All simulations of COQ9 were performed using the crystal structure of COQ9 where the α10 is in an extended conformation (PDB: 6AWL, chain A). Simulations of COQ7 were performed using a homology model of COQ7 (see below). For visualization purposes, selected frames from the CG-MD simulations were backmapped into atomistic coordinates using *backward.py*

(Wassenaar et al., 2014). Images were produced with PyMOL (Schrödinger LLC, Version 2.0) and videos were rendered with VMD (Humphrey et al., 1996; L DeLano, 2002).

**Protein-membrane systems:** CG-MD simulations based on the MARTINI force field have been previously used with success for different systems to investigate protein-lipid interactions (Periole et al., 2007; Schafer et al., 2011; Stansfeld et al., 2009; van den Bogaart et al., 2011). In CG-MD simulation systems, the center of mass of COQ9 was 70 Å away from the surface of the membrane. Since the last 7 C-terminal residues of COQ9 were not solved in the crystal structure, these residues were built to be disordered using Modeller version 9.11 (Webb and Sali, 2017). Inner mitochondrial membrane (IMM) models were built according to the CL composition of mammalian mitochondria, namely 10 to 20% of total mitochondrial phospholipids (Daum, 1985). Therefore, IMM mimics were featuring a lipid concentration of 16% CL/41% POPC/37% POPE/6% DSPC, while generic membrane models featuring 100% POPC lipids were built as control. Lipid bilayers of 160 × 160 $Å^2$ were generated using the insane (INSert membrANE) method of MARTINI (Wassenaar et al., 2015). Systems were solvated with polarizable CG water, and ions were added to the system to obtain a 150 mM NaCl aqueous solution, with extra ions added to neutralize the system. Following solvation, systems were energy minimized with a timestep of 5 fs. Successive equilibrations with decreasing restraints were performed in order to obtain a fully equilibrated system (force constants of 1000, 500, 250 and 0 kJ/mol applied on protein particles, 10 ns of runs with a timestep of 5 fs for each). In the production phase (10 μs of run with a timestep of 15 fs), the protein, membrane and the aqueous phase (water and ions) were coupled independently to an external bath at 310 K and 1 bar. Three MD repeats with randomized initial velocities were performed for each membrane system and they yielded consistent results (Fig. 4A, S3G, S3H, S3I). The minimum pairwise distances between the protein and the membrane were calculated using the *gmx pairdist* tool of Gromacs (Van der Spoel et al., 2005), which takes into account the distance to the periodic image of the membrane. The MSD and lateral diffusion coefficients were calculated using the *gmx msd* tool of Gromacs (Van der Spoel et al., 2005). Average occupancies of lipids were calculated using VMD's VolMap plugin and visualized using VMD (Humphrey et al., 1996). CG-MD simulations of COQ7 were performed to investigate the binding of COQ7 to 130 × 130 $Å^2$ IMM models (16% CL/41% POPC/37% POPE/6% DSPC). The procedure applied to COQ9 was used.

**Protein in water systems:** The MARTINI force field allows protein tertiary arrangements, whereas local secondary structure is predefined and imposed. COQ9 was solvated with polarizable CG water and ions were added to the system to obtain a 150 mM NaCl aqueous solution, with extra ions added to neutralize the system. Following solvation, systems were energy minimized with a timestep of 5 fs. Successive equilibrations with decreasing restraints were performed in order to obtain a fully equilibrated system (force constants of 1000, 500, 250 and 0 kJ/mol applied on protein particles, 10 ns of runs with a timestep of 5 fs for each). In the production phase (10 μs of run with a timestep of 15 fs), the protein and the aqueous phase (water and ions) were coupled independently to an external bath at 310 K and no pressure coupling was applied.

## Bioinformatics, docking, and modeling

**Bioinformatics Analysis of Secondary Structures of TFR proteins:** Secondary structures were assigned to the representative set of TFR sequences as defined by Yu and colleagues (Yu et al., 2010b) and to COQ9 using ICM-Pro molecular modeling software (Abagyan et al., 1994). Each helix was aligned and centered independently for all the reference TFRs, and the mean helix length and the standard deviation was computed for each helix. This analysis therefore does not take into account loop regions. For each residue position of each helix the percentage of TFRs having a residue that belongs to this helix was calculated.

**Ligand Docking:** Ligand docking and scoring was performed using the ICM-Pro molecular modeling software (Abagyan and Totrov, 1994; Abagyan et al., 1994). ICM ligand docking is based on biased probability Monte Carlo (BPMC) optimization of the ligand internal coordinates in the set of grid potential maps of the receptor, where the grid potential maps account for van der Waals, hydrogen-bonding, hydrophobic, and electrostatic interactions between ligand and receptor. The crystal structure of COQ9 where the α10 is in an extended conformation (PDB: 6AWL, chain A) was used as the receptor. $DMQ_5$ was used as the ligand instead of $DMQ_{10}$ because part of the hydrophobic tail of $DMQ_{10}$ is expected to reside in the membrane and because using such a long ligand increases the degrees of freedom and decreases the docking accuracy. The ligand was represented as an all-atom model and considered fully flexible. The standard docking procedure of ICM was used without the use of any experimentally derived information. Docking poses were evaluated with the ICM ligand binding score:

$$S_{bind} = E_{int} + T\Delta S_{Tor} + E_{vdw} + \alpha_1 E_{el} + \alpha_2 E_{hb} + \alpha_3 E_{hp} + \alpha_4 E_{sf}$$

where $E_{int}$ is the internal strain of the ligand, $T = 300$ K, $\Delta S_{Tor}$ is the conformational entropy loss of the ligand upon binding, $\alpha_i$ are constants independent from the ligand and receptor. $E_{vdw}$, $E_{el}$, $E_{hb}$, $E_{hp}$, $E_{sf}$ are van der Waals, electrostatic, hydrogen bonding, and nonpolar and polar atom solvation energy differences between bound and unbound states, respectively. To compare the docking pose to the co-crystallized isoprenes (PDB: 6DEW), chains A-F and co-crystallizing isoprenes were superimposed to the docked complex. The RMSD between the isoprene chain of $DMQ_5$ and that of farnesol (bound to chain A) were calculated on 15 matching carbon atoms and was found to be 1.5 Å. To visualize the $DMQ_5$-bound COQ9 on the membrane, the globular domain of COQ9 was superimposed in the docked complex to the globular domain of COQ9 in a membrane-bound state obtained from the CG-MD simulation. Since the ligand found contacts with W240 in the docking procedure, the crystal structure conformation of W240 (PDB: 6AWL, chain A) was used for the membrane-bound state of COQ9 for visualization purposes in Figure S5C.

**Homology Modeling of COQ7:** At present, there are no crystal structures available for human COQ7. Pfam (Finn et al., 2016) identifies COQ7 as a di-iron carboxylate protein that belongs to the ferritin-like superfamily. Members of this protein family are known to have a four-helix bundle folding architecture with a conserved iron binding motif (Stenmark et al., 2001a). Several attempts were previously made to model Coq7 homologues (*P. aeruginosa*, *R. norvegicus*, *S. cerevisiae*) using homology modeling techniques (Busso et al., 2015; Rea,

2001; Stenmark et al., 2001a). Here, we used a similar approach to model the structure of COQ7 from *H. sapiens* starting from its sequence as obtained from the UniProt database (accession number Q99807) (Wu et al., 2006). SWISS-MODEL automated comparative protein modeling server (Schwede et al., 2003) was used in Automated Mode to construct a homology model of the human COQ7. The N-terminal 37 residues were removed from the sequence since they had low conservation and since this region was predicted to be disordered; the C-terminal 32 residues were not modeled since this region was missing in all found templates and was not included in the predicted four-helix bundle. SWISS-MODEL uses two scores for model evaluation: GMQE and QMEAN. GMQE (Global Model Quality Estimation) is expressed as a number between 0 and 1, and a higher value means higher model reliability. QMEAN (Benkert et al., 2011) estimates the quality of the model compared to experimental structures, and a higher value means better agreement between the model structure and experimental structures of similar size, where scores around zero indicate a good degree of nativeness and scores lower than or equal to −4.0 indicate a low quality model. The best template identified by SWISS-MODEL for COQ7 is a ferritin (PDB: 5HJH, 1.88 Å resolution), which has a 15% sequence identity to COQ7. The generated model has a GMQE score of 0.43 and QMEAN score of −3.09. Despite the initial low sequence identity with templates, COQ7 shares the well-defined structural fold of the ferritin-like superfamily (as determined by Pfam (Finn et al., 2016)). Therefore, modeling its four-helix bundle structure was facilitated by helical secondary structure prediction and the strong conservation of the iron binding motif. The resulting model was consistent with previously published models of Coq7p (Busso et al., 2015; Rea, 2001; Stenmark et al., 2001a).

**Homology Modeling of Coq9p:** COQ9 sequences from *H. sapiens* (accession number O75208) and *S. cerevisiae* (accession number Q05779) were obtained from the UniProt (Wu et al., 2006) database and were aligned using Clustal Omega (Sievers et al., 2011). This alignment was used to model yeast Coq9p with Modeller version 9.11 (Webb and Sali, 2017). The MD refinement parameter was turned off and 5 models were generated, where the model with the lowest molpdf score was chosen as the final model.

**Protein-protein docking:** To model the COQ9-COQ7 complex, the protein-protein docking server ZDock was used (Pierce et al., 2014). In predicting protein-protein complexes, ZDock takes into account shape complementarity, electrostatics and desolvation free energy (Chen et al., 2003). The crystal structure of COQ9, where the α10 is in an extended conformation (PDB: 6AWL, chain A), and the homology model generated for COQ7 were used as input structures. Protein-protein docking was guided by (i) the experimental data (Fig. S4A), where residues that disrupted binding were forced to be included in the interface and residues that did not affect binding were forced not to be included and (ii) the preferred membrane orientation of COQ9 and COQ7 as obtained from CG-MD simulations. Ten poses were obtained where the intermolecular contacts of Fig. S4A were fulfilled and the ZDock score of the least favored pose was lower by at most 30% of the best pose. Seven of the ten complex conformations were not occluding the membrane binding surface of COQ9 as identified through CG-MD simulations, and the top two conformations of this cluster were not occluding the membrane binding surface of COQ7.

These two conformations showed only minor differences and an equivalent complex architecture having an RMSD as low as 5.2 Å. The best ZDock pose between these two conformations was therefore used as representative of COQ9-COQ7 interactions and is reported in Figure 5.

**Liquid chromatography mass spectrometry lipidomics—**LC-MS samples contained either lipid extractions of *S. cerevisiae* pellets (either $1\times10^8$ cells or 50 mL of $OD_{600}$=3), *E. coli* pellets ($1\times10^{10}$ cells), $His_8$-MBP-tagged protein (40 nmols), or Coq9p-FLAG protein (normalized to an equal amount by gel quantitation) prepared as described elsewhere. LC-MS analysis was performed on an Acquity CSH C18 column held at 50 °C (100 mm × 2.1 mm × 1.7 μm particle size; Waters) using a Vanquish Binary Pump (400 μL/min flow rate; Thermo Scientific). Mobile phase A consisted of 10 mM ammonium acetate in ACN/H2O (70:30, v/v) containing 250 μL/L acetic acid. Mobile phase B consisted of 10 mM ammonium acetate in IPA/ACN (90:10, v/v) with the same additives. Mobile phase B was initially held at 2% for 2 min and then increased to 30% over 3 min. Mobile phase B was further increased to 50% over 1 min and 85% over 14 min and then raised to 99% over 1 min and held for 7 min. The column was reequilibrated for 2 min before the next injection. Ten microliters of sample were injected by a Vanquish Split Sampler HT autosampler (Thermo Scientific). The LC system was coupled to a Q Exactive mass spectrometer by a HESI II heated ESI source kept at 325 °C (Thermo Scientific). The inlet capillary was kept at 300 °C, sheath gas was set to 25 units, auxiliary gas to 10 units, and the spray voltage was set to 4,000/5,000 V. For targeted analysis the MS was operated in positive parallel reaction monitoring (PRM) mode and negative targeted single ion monitoring (t-SIM) acquiring scheduled, targeted scans to CoQ intermediates: PPAB, DMQ, CoQ. For discovery analysis, the MS was operated in polarity switching dd-MS2 mode. MS acquisition parameters were 17,500 resolving power, $3\times10^6$ automatic gain control (AGC) target for $MS^1$ and $5\times10^5$ AGC target for $MS^2$ scans, 100-ms $MS^1$ and 35-ms $MS^2$ ion accumulation time, 240- to 1,600-Th $MS^1$ scan range, 1.4-Th isolation width for fragmentation, stepped HCD collision energy (20, 25/30 units), 1.0% under fill ratio, and 10-s dynamic exclusion.

For extended CoQ intermediate detection (Figure S6D) the LC-MS was performed as described above, with the following differences: Acquity CSH C18 column (150 mm × 2.1 mm × 1.7 μm particle size); Vanquish Binary Pump (250 μL/min flow rate); ACN/H2O (90:10, v/v) in Mobile phases A and B; Mobile phase B increased from 65–99% over 9 min, held at 99% (2 min), then returned to 65% over 0.5 min, column re-equilibration (2.5 min); Q Exactive HF mass spectrometer; HESI II heated ESI source (300 °C); S -lens RF level to 50.0 and spray voltage set to 4,000 V for positive and 3,500 V for negative modes. MS was operated in positive and negative PRM mode, respectively, acquiring targeted scants to detect CoQ intermediates: 4-HP, PPHB, PPAB, 4-AP, HHAB, DDMQ, DMQ, IDMQ, $CoQ_6$, $CoQ_{10}$. MS acquisition parameters were 60,000 resolving power for $MS^2$ scans, $5\times10^5$ AGC, 200-ms $MS^2$ ion accumulation time, 2.2-Th isolation width for fragmentation, and stepped HCD collision energy of 15, 25, and 35 units.

**Data analysis:** The resulting CoQ intermediate data were processed using TraceFinder 4.0 (Thermo Fisher Scientific). The resulting discovery lipidomics raw files were converted to mgf files via MSConvertGUI (ProteoWizard, Dr. Parag Mallick, Stanford University) and processed using Compound Discoverer 2.0 (Thermo Fisher Scientific) and an in-house developed software suite, LipiDex (Hutchins, 2018). All raw files were loaded into Compound Discoverer with blanks marked as such to generate two result files using the following Workflow Processing Nodes: Input Files, Select Spectra, Align Retention Times, Detect Unknown Compounds, Group Unknown Compounds, Fill Gaps and Mark Background Compounds for the so called "Aligned" result and solely Input Files, Select Spectra, and Detect Unknown Compounds for an "Unaligned" Result. Under Select Spectra, scan type was set to Full and unrecognized mass analyzer replacement to FTMS, the retention time limits were set between 0.4 and 21 min, MS order as well as unrecognized MS order replacements were set to MS1. Under Align Retention Times the mass tolerance was set to 10 ppm and the maximum shift according to the dataset to either 0.8 min. Under Detect Unknown Compounds, the mass tolerance was also set to 10 ppm, with an S/N threshold of 3, and a minimum peak intensity of 5E4. Further, [M+H]+1 and [M-H]-1 were selected as ions and a maximum peak width of 0.75 min as well as a minimum number of scans per peak equaling 5 were set. Lastly, for Group Unknown Compounds as well as Fill Gaps, mass tolerance was set to 10 ppm and retention time tolerance to 0.2 minutes. For best compound selection rules #1 and #2 were set to "unspecified," while MS1 was selected for preferred MS order and [M+H]+1 as the preferred ion. For everything else, the default settings were used. Resulting peak tables were exported as excel files in three levels of Compounds, Compound per File and Features (just Features for the "Unaligned") and later saved as csvs. Normalization and enrichments calculations were performed as specified in the Spreadsheet S2. *p*-values were calculated via Student's T Test assuming two-tailed distributions and equal variance.

## Sample preparation for *S. cerevisiae* lipids enriched in Coq9p$^{FLAG}$ pull-downs

**Coq9p$^{FLAG}$ expression and immunoprecipitation:** *S. cerevisiae* (BY4742) expressing p416GPD Coq9p-FLAG were grown in Ura$^-$ synthetic complete media with 1% glucose (1L inoculated with $1\times10^8$ cells in triplicate, 30 °C, 220 rpm), harvested by centrifugation (4,000×g, 5 min, 25 °C) 4 hours post diauxic shift, frozen in $N_{2(l)}$, and stored at −80 °C. Yeast pellets ($1\times10^8$ cells in triplicate) containing overexpressed protein were harvested in parallel.

Yeast spheroplasts were prepared as previously described (Boldogh and Pon, 2007). Yeast pellets were resuspended in 35 mL of pretreatment buffer (0.1 M Tris$SO_4$, pH 9.4, 10 mM DTT), incubated (30 °C, 220 rpm, 15 min), and pelle ted by centrifugation (1,500×g, 5 min). Pellets were resuspended in SP buffer (1.2 M Sorbitol, 20 mM KPi, pH 7.4), zymolyase (7.5 mg zymolyse per g pellet, MP Biomedicals 0832092) was added, and incubated (30 °C, 220 rpm, 40 min). Yeast spheroplasts were pelleted by centrifugation (4,500×g, 5 min, 4 °C), washed with 40 mL SP buffer, and pelleted by centrifugation (4,500×g, 5 min, 4 °C). Yeast spheroplasts were resuspended in 25 mL lysis buffer with protease inhibitors (10 mM TrisCl pH 8.0, 1 mM EDTA, 0.5 mM EGTA, 140 mM NaCl, 1 mM PMSF and peptide protease inhibitors: 500 ng/mL leupeptin hemisulfate, pepstatin A, chymostatin, aprotinin, and

antipain dihydrochloride at pH 7.2) and lysed by sonication (3 pulses of 15 sec). Digitonin in lysis buffer (0.4% w/v final digitonin) was added and lysate was incubated (4 °C , 30 min, nutating) then clarified by centrifugation (15,000×g, 30 min, 4 °C). Clarified lysate was added to 300 μL FLAG-conjugated magnetic bead slurry (Sigma M8823) equilibrated with lysis buffer and incubated (4 °C, 2.5 hrs, end-over-end). FLAG beads were pelleted by centrifugation (700×g, 3 min, 4 °C), resuspended in lysis buffer (1 mL), washed 5X in lysis buffer with 0.4% digitonin, and washed 2X in lysis buffer without digitonin with magnetization. Protein was eluted into 1 mL of elution buffer (10 mM TrisCl pH 8.0, 1 mM EDTA, 0.5 mM EGTA, 140 mM NaCl, and 0.2 mg/mL FLAG peptide, Sigma F3290) with gentle agitation (1 hr, 25 °C).

**Lipid extraction:** Immuno-purified Coq9p-FLAG (triplicates normalized to the lowest concentration by gel quantification) was thawed and buffer (10 mM TrisHCl pH 7.8, 140 mM NaCl) was added to 580 μL and vortexed (30 s). Extraction was initiated by $CH_3Cl$:MeOH (1:1, v/v, 3 mL) and vortexing (2×30 s). Samples were acidified to pH 0.5–2 (100 μL 1 M HCl) and mixed by vortexing (2×30 s). Phase separation was completed by centrifugation (3,220×g, 2 min, 4 °C), and the organic layer (1.5 mL) was tran sferred to a new 1.5 tubes and dried under $Ar_{(g)}$. The dried lipids were reconstituted in ACN/IPA/$H_2O$ (65:35:5, v/v/v, 50 μL) by vortexing (2×30 s), transferred to a sample vial and stored under $Ar_{(g)}$ at −80 C. Frozen yeast pellets ($1\times10^8$ cells by $OD_{600}$) were extracted similarly with the following exceptions: glass beads (0.5 mm diameter, 100 μL) added upon thawing, 900 μL of $CH_3Cl$:MeOH, 200 μL 1 M HCl and 400 μL of organic transferred.

### Sample preparation for *E. coli* lipids co-purifying with $His_8$-MBP-$COQ9^{N\Delta79}$

**Sample preparation:** $His_8$-MBP-[TEV]-$COQ9^{N\Delta79}$, $His_8$-MBP-[TEV]-$COQ9^{N\Delta79,W240K}$, $His_6$-MBP proteins were expressed and purified as described in "$COQ9^{N\Delta79}$ and $COQ9^{N\Delta79,\ C\Delta31}$ expression and purification" from 1L of *E. coli* in triplicate. Upon *E. coli* harvest, cell pellets ($1\times10^{10}$ cells by $OD_{600}$) were collected in triplicate. Upon protein collection, the elution was performed in a column, collected in 1 mL aliquots by gravity flow, and frozen in $N_{2(l)}$, and stored at −80 °C for lipid extraction at the first IMAC elution.

**Lipid extraction:** Cell pellets were thawed on ice, resuspended in 400 μL PBS by vortexing (30 s). Purified protein (40 nmol by $A_{280}$) was brought to 456 μL in 50 mM Tris pH 7.4, 200 mM NaCl, 100 mM imidazole. The aqueous samples were transferred to clean glass tubes and lipid extraction was initiated by addition of $CH_3Cl$:MeOH (1:1, v/v, 5 mL) and vortexing (30 s) to form a single phase. Samples were acidified to pH 0.5–2 (250 μL 1 M HCl) and mixed by vortexing (1×30 s, 1×15 s). After inducing phase separation by addition of 500 μL of brine, vortexing (15 s), and centrifugation (1,800×g, 4 min, 4 °C), the aqueous layer was aspirated, and organic layer dried under $Ar_{(g)}$. The dried lipids were reconstituted in ACN/IPA/$H_2O$ (65:35:5, v/v/v, 100 μL) by vortexing (2×30 s), transferred to a sample vial, and stored under $Ar_{(g)}$ at −80 C.

### Sample preparation for CoQ intermediates in *S. cerevisiae*

**Sample preparation:** (A) For PPAB, CoQ, DMQ detection (Figure 6E): *S. cerevisiae* (WT BY4742) expressing plasmids encoding Coq9p-FLAG variants in p416GPD were cultured

as described previously (Stefely et al., 2016a). Yeast were grown in synthetic media ($Ura^-$) respiration media (0.1% glucose, 3% glycerol w/v) to early respiration growth. Specifically, 100 mL was inoculated with $2.5\times10^6$ cells, from 12 h overnight cultures grown in $Ura^-$ 2% glucose, and incubated at 30 °C for 25 h at 230 rpm. Cells w ere grown and harvested in triplicate ($1\times10^8$ cells by $OD_{600}$) by centrifugation (3,000×*g*, 3 min, 4 °C) (Hebert et al., 2013). The supernat ant was aspirated and pellets frozen in $N_{2(l)}$ and stored at −80 °C.

(B) For extended CoQ intermediate detection (Figure S6D): *S. cerevisiae* (WT BY4742) expressing plasmids encoding Coq9p-FLAG variants in p416GPD or Coq8p-FLAG in p413GPD were cultured as described previously (Marbois et al., 2010) (Xie et al., 2012). Yeast were grown in synthetic media ($Ura^-His^-$) fermentation media (2% galactose, 0.1% dextrose, 100 μM pABA). Specifically, 50 mL was inoculated with 6 mL pABA-starved yeast in stationary phase and incubated at 30 °C at 230 rpm until OD ~3. Cell s were grown and harvested in triplicate (50 mL of $OD_{600}$=3 cells) by centrifugation (3,000×*g*, 3 min, 4 °C).

**Lipid extraction:** (A) For PPAB, CoQ, DMQ detection (Figure 6E): Frozen yeast pellets ($1\times10^8$ cells) were thawed on ice and mixed with glass beads (0.5 mm diameter, 100 μL). $CHCl_3$/MeOH (1:1, v/v, 4 °C, 900 μL) was added and samples were vortexed (2×30 s). HCl (1 M, 200 μL, 4 °C) was added and samples vortexed (2×30 s). The samples were centrifuged (5,000 *g*, 2 min, 4 °C) to complete phase separation. 400 μL of the organic phase was transferred to a clean tube and dried under $Ar_{(g)}$. The organic residue was reconstituted in ACN/IPA/$H_2O$ (65:30:5, v/v/v) (100 μL) for LC–MS analysis.

(B) For extended CoQ intermediate detection (Figure S6D): Yeast pellets were resuspended in water (100 μL) and submitted to a Soxhlet extraction with added internal standard ($CoQ_{10}$, 1μM in final reconstitution) as described previously (Marbois et al., 2010) (Xie et al., 2012). Aqueous sample was submitted to two iterative extractions: vortexed (30s) with methanol (1 mL) and petroleum ether (2 mL). The organic phases were transferred to a clean tube and dried under $Ar_{(g)}$. The organic residue was reconstituted in ACN/IPA/$H_2O$ (65:30:5, v/v/v) (200 μL) for LC–MS analysis.

## LC-MS/MS proteomics analysis of *S. cerevisiae*

**Sample preparation:** Frozen yeast pellets ($1\times10^8$ cells) were re-suspended in 100 μL guanidine-HCl (6M) and boiled for five minutes at 100 °C. Met hanol was added to a concentration of 90% to precipitate protein and the sample was centrifuged for 10 min at 14,000×g. The resulting pellet was re-suspended in 100 μL lysis buffer (8 M Urea, 100 mM Tris, 20 mM TCEP, 80 mM Chloroacetamide) and diluted with 1 mL 50 mM Tris. Protein digestion was performed overnight with trypsin (4 μg) and centrifuged the following morning for 5 min at 14,000×g prior to de-salting resulting supernatant with Strata C18 solid phase extraction cartridges. Peptides were dried in a vacuum centrifuge before re-suspending in 0.2% formic acid and quantified using Pierce Quantitative Colorimetric Peptide Assay (Thermo Fisher Scientific).

**LC-MS/MS label-free proteomics:** Samples were analyzed using an LC-MS instrument comprising an Orbitrap Fusion Lumos Tribrid mass spectrometer (Thermo Fisher Scientific)

and an Ultimate 3000 RSLCnano chromatography system. Mobile phase A consisted of 0.2% formic acid in water and mobile phase B consisted of 0.2% formic acid in acetonitrile. A 75-min gradient ranging from 0% to 50% B was employed spanning a total runtime of 90 min. 2 μg analytes were injected onto a 1.7 micron C18 column packed in-house to a length of 35 cm and heated to 55 °C. Survey scans of peptide precursors were collected from 350–1350 Th with an AGC target of 1,000,000 and a resolution of 60,000 in the Orbitrap followed by HCD MS/MS scans taken at top speed in the ion trap.

The resulting LC-MS proteomics data were processed using Maxquant software version 1.5.2.8 and searched against a *S. cerevisiae* database downloaded from Uniprot on 8/10/16 (Cox et al., 2014; Cox and Mann, 2008; Cox et al., 2011). The digestion enzyme was set to trypsin with up to two missing cleavages, carbamidomethylation of cysteine as a fixed modification, and oxidation of methionine and protein N-terminal acetylation as variable modifications. The match between runs feature was utilized to decrease missing data values within the data set. Precursor mass tolerance was 20 ppm and product ions were searched at 0.5 Da tolerances. Peptides were filtered to a 1% FDR and combined to protein groups based on the rules of parsimony.

### QUANTIFICATION AND STATISTICAL ANALYSIS

See each individual method for the associated statistical analysis. The majority of *p*-values in this report were calculated using an unpaired, two-tailed, Student's *t*-test. MS data analysis was performed as described in each MS analysis section and in Spreadsheet S2. In all cases, *n* represents independent replicates of an experiment and error bars represent standard deviation.

## Supplementary Material

Refer to Web version on PubMed Central for supplementary material.

## ACKNOWLEDGEMENTS

We thank members of the Pagliarini laboratory and Alessio Prunotto for helpful discussions as well as Amy Lin for her assistance with figure generation. Research reported in this publication was supported by the National Institute of General Medical Sciences of the National Institutes of Health under award numbers R01GM115591 (to D.J.P.), T32GM08349 (to D.C.L.), and R35GM118110 and P41GM108538 (to J.J.C.). This work was further supported by National Science Foundation Graduate Research Fellowship DGE-1256259 (to D.C.L.), and the Swiss National Science Foundation (grant 31003A_170154 to M.D.P.). Crystallization studies were performed at the Collaborative Crystallography Core in the Department of Biochemistry at the University of Wisconsin-Madison (C3DB). This research used resources of the Advanced Photon Source, a U.S. Department of Energy (DOE) Office of Science User Facility operated for the DOE Office of Science by Argonne National Laboratory under Contract No. DE-AC02–06CH11357. Use of the LS-CAT Sector 21 was supported by the Michigan Economic Development Corporation and the Michigan Technology Tri-Corridor (Grant 085P1000817). GM/CA@APS has been funded in whole or in part with Federal funds from the National Cancer Institute (ACB-12002) and the National Institute of General Medical Sciences (AGM-12006).

## REFERENCES

Abagyan R, and Totrov M (1994). Biased Probability Monte-Carlo Conformational Searches and Electrostatic Calculations for Peptides and Proteins. Journal of Molecular Biology 235, 983–1002. [PubMed: 8289329]

Abagyan R, Totrov M, and Kuznetsov D (1994). Icm - a New Method for Protein Modeling and Design - Applications to Docking and Structure Prediction from the Distorted Native Conformation. Journal of computational chemistry 15, 488–506.

Abraham MJ, Murtola T, Schulz R, Páll S, Smith JC, Hess B, and Lindahl E (2015). GROMACS: High performance molecular simulations through multi-level parallelism from laptops to supercomputers. SoftwareX 1–2, 19–25.

Acehan D, Malhotra A, Xu Y, Ren M, Stokes DL, and Schlame M (2011). Cardiolipin affects the supramolecular organization of ATP synthase in mitochondria. Biophys J 100, 2184–2192. [PubMed: 21539786]

Adams PD, Afonine PV, Bunkoczi G, Chen VB, Davis IW, Echols N, Headd JJ, Hung LW, Kapral GJ, Grosse-Kunstleve RW, et al. (2010). PHENIX: a comprehensive Python-based system for macromolecular structure solution. Acta Crystallogr D 66, 213–221. [PubMed: 20124702]

Afonine PV, Grosse-Kunstleve RW, Echols N, Headd JJ, Moriarty NW, Mustyakimov M, Terwilliger TC, Urzhumtsev A, Zwart PH, and Adams PD (2012). Towards automated crystallographic structure refinement with phenix.refine. Acta Crystallogr D Biol Crystallogr 68, 352–367. [PubMed: 22505256]

Alattia JR, Shaw JE, Yip CM, and Prive GG (2006). Direct visualization of saposin remodelling of lipid bilayers. J Mol Biol 362, 943–953. [PubMed: 16949605]

Bai Y, McCoy JG, Levin EJ, Sobrado P, Rajashankar KR, Fox BG, and Zhou M (2015). X-ray structure of a mammalian stearoyl-CoA desaturase. Nature 524, 252–256. [PubMed: 26098370]

Bankaitis VA, Mousley CJ, and Schaaf G (2010). The Sec14 superfamily and mechanisms for crosstalk between lipid metabolism and lipid signaling. Trends in Biochemical Sciences 35, 150–160. [PubMed: 19926291]

Behan RK, and Lippard SJ (2010). The Aging-Associated Enzyme CLK-1 Is a Member of the Carboxylate-Bridged Diiron Family of Proteins. Biochemistry 49, 9679–9681. [PubMed: 20923139]

Benkert P, Biasini M, and Schwede T (2011). Toward the estimation of the absolute quality of individual protein structure models. Bioinformatics 27, 343–350. [PubMed: 21134891]

Boldogh IR, and Pon LA (2007). Purification and subfractionation of mitochondria from the yeast Saccharomyces cerevisiae. Mitochondria, 2nd Edition 80, 45–64.

Busso C, Ferreira JR, Paulela JA, Bleicher L, Demasi M, and Barros MH (2015). Coq7p relevant residues for protein activity and stability. Biochimie 119, 92–102. [PubMed: 26497406]

Chan DI, and Vogel HJ (2010). Current understanding of fatty acid biosynthesis and the acyl carrier protein. Biochemical Journal 430, 1–19. [PubMed: 20662770]

Chen R, Li L, and Weng ZP (2003). ZDOCK: An initial-stage protein-docking algorithm. Proteins-Structure Function and Genetics 52, 80–87.

Chua NK, Howe V, Jatana N, Thukral L, and Brown AJ (2017). A conserved degron containing an amphipathic helix regulates the cholesterol-mediated turnover of human squalene monooxygenase, a rate-limiting enzyme in cholesterol synthesis. J Biol Chem 292, 19959–19973. [PubMed: 28972164]

Connerth M, Tatsuta T, Haag M, Klecker T, Westermann B, and Langer T (2012). Intramitochondrial transport of phosphatidic acid in yeast by a lipid transfer protein. Science 338, 815–818. [PubMed: 23042293]

Cornell RB (2016). Membrane lipid compositional sensing by the inducible amphipathic helix of CCT. Biochim Biophys Acta 1861, 847–861. [PubMed: 26747646]

Cox J, Hein MY, Luber CA, Paron I, Nagaraj N, and Mann M (2014). Accurate proteome-wide label-free quantification by delayed normalization and maximal peptide ratio extraction, termed MaxLFQ. Mol Cell Proteomics 13, 2513–2526. [PubMed: 24942700]

Cox J, and Mann M (2008). MaxQuant enables high peptide identification rates, individualized p.p.b.-range mass accuracies and proteome-wide protein quantification. Nat Biotechnol 26, 1367–1372. [PubMed: 19029910]

Cox J, Neuhauser N, Michalski A, Scheltema RA, Olsen JV, and Mann M (2011). Andromeda: a peptide search engine integrated into the MaxQuant environment. Journal of proteome research 10, 1794–1805. [PubMed: 21254760]

Crosby J, and Crump MP (2012). The structural role of the carrier protein - active controller or passive carrier. Nat Prod Rep 29, 1111–1137. [PubMed: 22930263]

Cuthbertson L, and Nodwell JR (2013). The TetR family of regulators. Microbiol Mol Biol Rev 77, 440–475. [PubMed: 24006471]

Danhauser K, Herebian D, Haack TB, Rodenburg RJ, Strom TM, Meitinger T, Klee D, Mayatepek E, Prokisch H, and Distelmaier F (2016). Fatal neonatal encephalopathy and lactic acidosis caused by a homozygous loss-of-function variant in COQ9. Eur J Hum Genet 24, 450–454. [PubMed: 26081641]

Daum G (1985). Lipids of Mitochondria. Biochimica Et Biophysica Acta 822, 1–42. [PubMed: 2408671]

Drin G, Casella JF, Gautier R, Boehmer T, Schwartz TU, and Antonny B (2007). A general amphipathic alpha-helical motif for sensing membrane curvature. Nat Struct Mol Biol 14, 138–146. [PubMed: 17220896]

Duncan AJ, Bitner-Glindzicz M, Meunier B, Costello H, Hargreaves IP, Lopez LC, Hirano M, Quinzii CM, Sadowski MI, Hardy J, et al. (2009). A nonsense mutation in COQ9 causes autosomal-recessive neonatal-onset primary coenzyme Q10 deficiency: a potentially treatable form of mitochondrial disease. Am J Hum Genet 84, 558–566. [PubMed: 19375058]

Emsley P, Lohkamp B, Scott WG, and Cowtan K (2010). Features and development of Coot. Acta Crystallogr D Biol Crystallogr 66, 486–501. [PubMed: 20383002]

Fazakerley DJ, Chaudhuri R, Yang P, Maghzal GJ, Thomas KC, Krycer JR, Humphrey SJ, Parker BL, Fisher-Wellman KH, Meoli CC, et al. (2018). Mitochondrial CoQ deficiency is a common driver of mitochondrial oxidants and insulin resistance. Elife 7.

Finn RD, Coggill P, Eberhardt RY, Eddy SR, Mistry J, Mitchell AL, Potter SC, Punta M, Qureshi M, Sangrador-Vegas A, et al. (2016). The Pfam protein families database: towards a more sustainable future. Nucleic Acids Res 44, D279–D285. [PubMed: 26673716]

Furst W, and Sandhoff K (1992). Activator proteins and topology of lysosomal sphingolipid catabolism. Biochim Biophys Acta 1126, 1–16. [PubMed: 1606169]

Garcia-Corzo L, Luna-Sanchez M, Doerrier C, Garcia JA, Guaras A, Acin-Perez R, Bullejos-Peregrin J, Lopez A, Escames G, Enriquez JA, et al. (2013). Dysfunctional Coq9 protein causes predominant encephalomyopathy associated with CoQ deficiency. Hum Mol Genet 22, 1233–1248. [PubMed: 23255162]

Gietz RD, and Woods RA (2002). Transformation of yeast by lithium acetate/single-stranded carrier DNA/polyethylene glycol method. Method Enzymol 350, 87–96.

Gohil VM, Hayes P, Matsuyama S, Schagger H, Schlame M, and Greenberg ML (2004). Cardiolipin biosynthesis and mitochondrial respiratory chain function are interdependent. J Biol Chem 279, 42612–42618. [PubMed: 15292198]

Gonzalez-Mariscal I, Garcia-Teston E, Padilla S, Martin-Montalvo A, Pomares-Viciana T, Vazquez-Fonseca L, Gandolfo-Dominguez P, and Santos-Ocana C (2014). Regulation of coenzyme Q biosynthesis in yeast: a new complex in the block. IUBMB Life 66, 63–70. [PubMed: 24470391]

Grabon A, Orlowski A, Tripathi A, Vuorio J, Javanainen M, Rog T, Lonnfors M, McDermott MI, Siebert G, Somerharju P, et al. (2017). Dynamics and energetics of the mammalian phosphatidylinositol transfer protein phospholipid exchange cycle. Journal of Biological Chemistry 292, 14438–14455. [PubMed: 28718450]

He CH, Black DS, Nguyen TP, Wang C, Srinivasan C, and Clarke CF (2015). Yeast Coq9 controls deamination of coenzyme Q intermediates that derive from para-aminobenzoic acid. Biochim Biophys Acta 1851, 1227–1239. [PubMed: 26008578]

He CH, Xie LX, Allan CM, Tran UC, and Clarke CF (2014). Coenzyme Q supplementation or over-expression of the yeast Coq8 putative kinase stabilizes multi-subunit Coq polypeptide complexes in yeast coq null mutants. Biochim Biophys Acta 1841, 630–644. [PubMed: 24406904]

Hebert AS, Merrill AE, Stefely JA, Bailey DJ, Wenger CD, Westphall MS, Pagliarini DJ, and Coon JJ (2013). Amine-reactive Neutron-encoded Labels for Highly Plexed Proteomic Quantitation. Mol Cell Proteomics 12, 3360–3369. [PubMed: 23882030]

Hill CH, Cook GM, Spratley SJ, Fawke S, Graham SC, and Deane JE (2018). The mechanism of glycosphingolipid degradation revealed by a GALC-SapA complex structure. Nat Commun 9, 151. [PubMed: 29323104]

Hofbauer HF, Gecht M, Fischer SC, Seybert A, Frangakis AS, Stelzer EHK, Covino R, Hummer G, and Ernst R (2018). The molecular recognition of phosphatidic acid by an amphipathic helix in Opi1. Journal of Cell Biology 217, 3109–3126. [PubMed: 29941475]

Hsieh EJ, Gin P, Gulmezian M, Tran UC, Saiki R, Marbois BN, and Clarke CF (2007). Saccharomyces cerevisiae Coq9 polypeptide is a subunit of the mitochondrial coenzyme Q biosynthetic complex. Arch Biochem Biophys 463, 19–26. [PubMed: 17391640]

Hughes BG, Harrison PM, and Hekimi S (2017). Estimating the occurrence of primary ubiquinone deficiency by analysis of large-scale sequencing data. Sci Rep 7, 17744. [PubMed: 29255295]

Humphrey W, Dalke A, and Schulten K (1996). VMD: Visual molecular dynamics. J Mol Graph Model 14, 33–38.

Hutchins PD (2018). LipiDex: An Integrated Software Package for High-Confidence Lipid Identification. Cell Systems 6.

Ikon N, and Ryan RO (2017). Cardiolipin and mitochondrial cristae organization. Biochim Biophys Acta 1859, 1156–1163.

Ile KE, Schaaf G, and Bankaitis VA (2006). Phosphatidylinositol transfer proteins and cellular nanoreactors for lipid signaling. Nature Chemical Biology 2, 576–583. [PubMed: 17051233]

Johnson A, Gin P, Marbois BN, Hsieh EJ, Wu M, Barros MH, Clarke CF, and Tzagoloff A (2005). COQ9, a new gene required for the biosynthesis of coenzyme Q in Saccharomyces cerevisiae. J Biol Chem 280, 31397–31404. [PubMed: 16027161]

Jurrus E, Engel D, Star K, Monson K, Brandi J, Felberg LE, Brookes DH, Wilson L, Chen JH, Liles K, et al. (2018). Improvements to the APBS biomolecular solvation software suite. Protein Science 27, 112–128. [PubMed: 28836357]

Kabsch W (2010). Xds. Acta Crystallogr D Biol Crystallogr 66, 125–132. [PubMed: 20124692]

Klock HE, Koesema EJ, Knuth MW, and Lesley SA (2008). Combining the polymerase incomplete primer extension method for cloning and mutagenesis with microscreening to accelerate structural genomics efforts. Proteins 71, 982–994. [PubMed: 18004753]

L DeLano W (2002). The PyMOL Molecular Graphics System (2002) DeLano Scientific, Palo Alto, CA, USA http://www.pymol.org.

Lahiri S, Toulmay A, and Prinz WA (2015). Membrane contact sites, gateways for lipid homeostasis. Curr Opin Cell Biol 33, 82–87. [PubMed: 25569848]

Lohman DC, Forouhar F, Beebe ET, Stefely MS, Minogue CE, Ulbrich A, Stefely JA, Sukumar S, Luna-Sanchez M, Jochem A, et al. (2014). Mitochondrial COQ9 is a lipid-binding protein that associates with COQ7 to enable coenzyme Q biosynthesis. Proc Natl Acad Sci U S A 111, E4697–4705. [PubMed: 25339443]

Lu TT, Lee SJ, Apfel UP, and Lippard SJ (2013). Aging-associated enzyme human clock-1: substrate-mediated reduction of the diiron center for 5-demethoxyubiquinone hydroxylation. Biochemistry 52, 2236–2244. [PubMed: 23445365]

Luna-Sanchez M, Diaz-Casado E, Barca E, Tejada MA, Montilla-Garcia A, Cobos EJ, Escames G, Acuna-Castroviejo D, Quinzii CM, and Lopez LC (2015). The clinical heterogeneity of coenzyme Q10 deficiency results from genotypic differences in the Coq9 gene. EMBO Mol Med 7, 670–687. [PubMed: 25802402]

Malinina L, Patel DJ, and Brown RE (2017). How alpha-Helical Motifs Form Functionally Diverse Lipid-Binding Compartments. Annu Rev Biochem 86, 609–636. [PubMed: 28375742]

Marbois B, Xie LX, Choi S, Hirano K, Hyman K, and Clarke CF (2010). para-Aminobenzoic acid is a precursor in coenzyme Q6 biosynthesis in Saccharomyces cerevisiae. J Biol Chem 285, 27827–27838. [PubMed: 20592037]

Marrink SJ, Risselada HJ, Yefimov S, Tieleman DP, and de Vries AH (2007). The MARTINI force field: Coarse grained model for biomolecular simulations. J Phys Chem B 111, 7812–7824. [PubMed: 17569554]

McAndrew RP, Wang Y, Mohsen AW, He M, Vockley J, and Kim JJ (2008). Structural basis for substrate fatty acyl chain specificity: crystal structure of human very-long-chain acyl-CoA dehydrogenase. J Biol Chem 283, 9435–9443. [PubMed: 18227065]

McCoy AJ, Grosse-Kunstleve RW, Adams PD, Winn MD, Storoni LC, and Read RJ (2007). Phaser crystallographic software. J Appl Crystallogr 40, 658–674. [PubMed: 19461840]

Metz G, Howard KP, Vanliemt WBS, Prestegard JH, Lugtenburg J, and Smith SO (1995). Nmr-Studies of Ubiquinone Location in Oriented Model Membranes - Evidence for a Single Motionally-Averaged Population. Journal of the American Chemical Society 117, 564–565.

Murley A, and Nunnari J (2016). The Emerging Network of Mitochondria-Organelle Contacts. Mol Cell 61, 648–653. [PubMed: 26942669]

Ozeir M, Pelosi L, Ismail A, Mellot-Draznieks C, Fontecave M, and Pierrel F (2015). Coq6 is responsible for the C4-deamination reaction in coenzyme Q biosynthesis in Saccharomyces cerevisiae. J Biol Chem 290, 24140–24151. [PubMed: 26260787]

Periole X, Cavalli M, Marrink SJ, and Ceruso MA (2009). Combining an Elastic Network With a Coarse-Grained Molecular Force Field: Structure, Dynamics, and Intermolecular Recognition. J Chem Theory Comput 5, 2531–2543. [PubMed: 26616630]

Periole X, Huber T, Marrink SJ, and Sakmar TP (2007). G protein-coupled receptors self-assemble in dynamics simulations of model bilayers. Journal of the American Chemical Society 129, 10126–10132. [PubMed: 17658882]

Pierce BG, Wiehe K, Hwang H, Kim BH, Vreven T, and Weng ZP (2014). ZDOCK server: interactive docking prediction of protein-protein complexes and symmetric multimers. Bioinformatics 30, 1771–1773. [PubMed: 24532726]

Pierrel F (2017). Impact of Chemical Analogs of 4-Hydroxybenzoic Acid on Coenzyme Q Biosynthesis: From Inhibition to Bypass of Coenzyme Q Deficiency. Front Physiol 8, 436. [PubMed: 28690551]

Prinz WA (2010). Lipid Trafficking sans Vesicles: Where, Why, How? Cell 143, 870–874. [PubMed: 21145454]

Ramos JL, Martínez-Bueno M, Molina-Henares AJ, Terán W, Watanabe K, Zhang X, Gallegos MT, Brennan R, and Tobes R (2005). The TetR family of transcriptional repressors. Microbiol Mol Biol Rev 69, 326–356. [PubMed: 15944459]

Rea S (2001). CLK-1/Coq7p is a DMQ mono-oxygenase and a new member of the di-iron carboxylate protein family. Febs Letters 509, 389–394. [PubMed: 11749961]

Reidenbach AG, Kemmerer ZA, Aydin D, Jochem A, McDevitt MT, Hutchins PD, Stark JL, Stefely JA, Reddy T, Hebert AS, et al. (2018). Conserved Lipid and Small-Molecule Modulation of COQ8 Reveals Regulation of the Ancient Kinase-like UbiB Family. Cell Chem Biol 25, 154–165 e111. [PubMed: 29198567]

Robertson RM, Yao JW, Gajewski S, Kumar G, Martin EW, Rock CO, and White SW (2017). A two-helix motif positions the lysophosphatidic acid acyltransferase active site for catalysis within the membrane bilayer. Nat Struct Mol Biol 24, 666-+. [PubMed: 28714993]

Rossmann M, Schultz-Heienbrok R, Behlke J, Remmel N, Alings C, Sandhoff K, Saenger W, and Maier T (2008). Crystal structures of human saposins C andD: implications for lipid recognition and membrane interactions. Structure 16, 809–817. [PubMed: 18462685]

Schafer LV, de Jong DH, Holt A, Rzepiela AJ, de Vries AH, Poolman B, Killian JA, and Marrink SJ (2011). Lipid packing drives the segregation of transmembrane helices into disordered lipid domains in model membranes. P Natl Acad Sci USA 108, 1343–1348.

Schwede T, Kopp J, Guex N, and Peitsch MC (2003). SWISS-MODEL: an automated protein homology-modeling server. Nucleic Acids Res 31, 3381–3385. [PubMed: 12824332]

Sievers F, Wilm A, Dineen D, Gibson TJ, Karplus K, Li WZ, Lopez R, McWilliam H, Remmert M, Soding J, et al. (2011). Fast, scalable generation of high-quality protein multiple sequence alignments using Clustal Omega. Mol Syst Biol 7.

Smith AC, Ito Y, Ahmed A, Schwartzentruber JA, Beaulieu CL, Aberg E, Majewski J, Bulman DE, Horsting-Wethly K, Koning DV, et al. (2018). A family segregating lethal neonatal coenzyme Q10 deficiency caused by mutations in COQ9. J Inherit Metab Dis

Srere PA (1985). The metabolon. Trends in Biochemical Sciences 10, 109–110.

Stansfeld PJ, Hopkinson R, Ashcroft FM, and Sansom MSP (2009). PIP2-Binding Site in Kir Channels: Definition by Multiscale Biomolecular Simulations. Biochemistry 48, 10926–10933. [PubMed: 19839652]

Stefely JA, Kwiecien NW, Freiberger EC, Richards AL, Jochem A, Rush MJP, Ulbrich A, Robinson KP, Hutchins PD, Veling MT, et al. (2016a). Mitochondrial protein functions elucidated by multi-omic mass spectrometry profiling. Nat Biotechnol 34, 1191–1197. [PubMed: 27669165]

Stefely JA, Licitra F, Laredj L, Reidenbach AG, Kemmerer ZA, Grangeray A, Jaeg-Ehret T, Minogue CE, Ulbrich A, Hutchins PD, et al. (2016b). Cerebellar Ataxia and Coenzyme Q Deficiency through Loss of Unorthodox Kinase Activity. Mol Cell 63, 608–620. [PubMed: 27499294]

Stefely JA, and Pagliarini DJ (2017). Biochemistry of Mitochondrial Coenzyme Q Biosynthesis. Trends Biochem Sci 42, 824–843. [PubMed: 28927698]

Stefely JA, Reidenbach AG, Ulbrich A, Oruganty K, Floyd BJ, Jochem A, Saunders JM, Johnson IE, Minogue CE, Wrobel RL, et al. (2015). Mitochondrial ADCK3 employs an atypical protein kinase-like fold to enable coenzyme Q biosynthesis. Mol Cell 57, 83–94. [PubMed: 25498144]

Stenmark P, Grunler J, Mattsson J, Sindelar PJ, Nordlund P, and Berthold DA (2001a). A new member of the family of di-iron carboxylate proteins - Coq7 (clk-1), a membrane-bound hydroxylase involved in ubiquinone biosynthesis. Journal of Biological Chemistry 276, 33297–33300. [PubMed: 11435415]

Stenmark P, Grunler J, Mattsson J, Sindelar PJ, Nordlund P, and Berthold DA (2001b). A new member of the family of di-iron carboxylate proteins. Coq7 (clk-1), a membrane-bound hydroxylase involved in ubiquinone biosynthesis. J Biol Chem 276, 33297–33300. [PubMed: 11435415]

Suetsugu S, Kurisu S, and Takenawa T (2014). Dynamic shaping of cellular membranes by phospholipids and membrane-deforming proteins. Physiol Rev 94, 1219–1248. [PubMed: 25287863]

Tamura Y, and Endo T (2017). Role of Intra- and Inter-mitochondrial Membrane Contact Sites in Yeast Phospholipid Biogenesis. Adv Exp Med Biol 997, 121–133. [PubMed: 28815526]

Tatsuta T, Scharwey M, and Langer T (2014). Mitochondrial lipid trafficking. Trends in Cell Biology 24, 44–52. [PubMed: 24001776]

Tran UC, and Clarke CF (2007). Endogenous synthesis of coenzyme Q in eukaryotes. Mitochondrion 7 Suppl, S62–71. [PubMed: 17482885]

Tran UC, Marbois B, Gin P, Gulmezian M, Jonassen T, and Clarke CF (2006). Complementation of Saccharomyces cerevisiae coq7 mutants by mitochondrial targeting of the Escherichia coli UbiF polypeptide: two functions of yeast Coq7 polypeptide in coenzyme Q biosynthesis. J Biol Chem 281, 16401–16409. [PubMed: 16624818]

Ulrich EL, Girvin ME, Cramer WA, and Markley JL (1985). Location and mobility of ubiquinones of different chain lengths in artificial membrane vesicles. Biochemistry 24, 2501–2508. [PubMed: 3839413]

van den Bogaart G, Meyenberg K, Risselada HJ, Amin H, Willig KI, Hubrich BE, Dier M, Hell SW, Grubmuller H, Diederichsen U, et al. (2011). Membrane protein sequestering by ionic protein-lipid interactions. Nature 479, 552–555. [PubMed: 22020284]

Van der Spoel D, Lindahl E, Hess B, Groenhof G, Mark AE, and Berendsen HJC (2005). GROMACS: Fast, flexible, and free. Journal of computational chemistry 26, 1701–1718. [PubMed: 16211538]

van Meer G, Voelker DR, and Feigenson GW (2008). Membrane lipids: where they are and how they behave. Nat Rev Mol Cell Bio 9, 112–124. [PubMed: 18216768]

Wang Y, Smith C, Parboosingh JS, Khan A, Innes M, and Hekimi S (2017). Pathogenicity of two COQ7 mutations and responses to 2,4-dihydroxybenzoate bypass treatment. J Cell Mol Med

Wassenaar TA, Ingolfsson HI, Bockmann RA, Tieleman DP, and Marrink SJ (2015). Computational Lipidomics with insane: A Versatile Tool for Generating Custom Membranes for Molecular Simulations. J Chem Theory Comput 11, 2144–2155. [PubMed: 26574417]

Wassenaar TA, Pluhackova K, Bockmann RA, Marrink SJ, and Tieleman DP (2014). Going Backward: A Flexible Geometric Approach to Reverse Transformation from Coarse Grained to Atomistic Models. J Chem Theory Comput 10, 676–690. [PubMed: 26580045]

Watanabe Y, Tamura Y, Kawano S, and Endo T (2015). Structural and mechanistic insights into phospholipid transfer by Ups1-Mdm35 in mitochondria. Nat Commun 6, 7922. [PubMed: 26235513]

Webb B, and Sali A (2017). Protein Structure Modeling with MODELLER. In Functional Genomics: Methods and Protocols, Kaufmann M, Klinger C, and Savelsbergh A, eds. (New York, NY: Springer New York), pp. 39–54.

Wessel D, and Flugge UI (1984). A method for the quantitative recovery of protein in dilute solution in the presence of detergents and lipids. Anal Biochem 138, 141–143. [PubMed: 6731838]

Wong LH, Copic A, and Levine TP (2017). Advances on the Transfer of Lipids by Lipid Transfer Proteins. Trends Biochem Sci 42, 516–530. [PubMed: 28579073]

Wu CH, Apweiler R, Bairoch A, Natale DA, Barker WC, Boeckmann B, Ferro S, Gasteiger E, Huang HZ, Lopez R, et al. (2006). The Universal Protein Resource (UniProt): an expanding universe of protein information. Nucleic Acids Res 34, D187–D191. [PubMed: 16381842]

Xie LTX, Hsieh EJ, Watanabe S, Allan CM, Chen JY, Tran UC, and Clarke CF (2011). Expression of the human atypical kinase ADCK3 rescues coenzyme Q biosynthesis and phosphorylation of Coq polypeptides in yeast coq8 mutants. Bba-Mol Cell Biol L 1811, 348–360.

Xie LX, Ozeir M, Tang JY, Chen JY, Jaquinod SK, Fontecave M, Clarke CF, and Pierrel F (2012). Overexpression of the Coq8 kinase in Saccharomyces cerevisiae coq null mutants allows for accumulation of diagnostic intermediates of the coenzyme Q6 biosynthetic pathway. J Biol Chem 287, 23571–23581. [PubMed: 22593570]

Yu F, He F, Yao H, Wang C, Wang J, Li J, Qi X, Xue H, Ding J, and Zhang P (2015). Structural basis of intramitochondrial phosphatidic acid transport mediated by Ups1-Mdm35 complex. EMBO Rep 16, 813–823. [PubMed: 26071601]

Yu Z, Reichheld SE, Savchenko A, Parkinson J, and Davidson AR (2010a). A comprehensive analysis of structural and sequence conservation in the TetR family transcriptional regulators. J Mol Biol 400, 847–864. [PubMed: 20595046]

Yu Z, Reichheld SE, Savchenko A, Parkinson J, and Davidson AR (2010b). A Comprehensive Analysis of Structural and Sequence Conservation in the TetR Family Transcriptional Regulators. Journal of Molecular Biology 400, 847–864. [PubMed: 20595046]

Zhang M, Mileykovskaya E, and Dowhan W (2005). Cardiolipin is essential for organization of complexes III and IV into a supercomplex in intact yeast mitochondria. J Biol Chem 280, 29403–29408. [PubMed: 15972817]

Zhang YX, Bharathi SS, Rardin MJ, Uppala R, Verdin E, Gibson BW, and Goetzman ES (2015). SIRT3 and SIRT5 Regulate the Enzyme Activity and Cardiolipin Binding of Very Long-Chain Acyl-CoA Dehydrogenase. Plos One 10.

## HIGHLIGHTS

- COQ9 specifically accesses and binds membrane-embedded aromatic isoprenes
- An exposed tryptophan and an amphipathic helix control lipid and membrane-binding
- Interactions with the peripheral membrane enzyme COQ7 suggest lipid presentation
- *In vivo* CoQ production relies on COQ9's membrane, lipid, and protein interactions

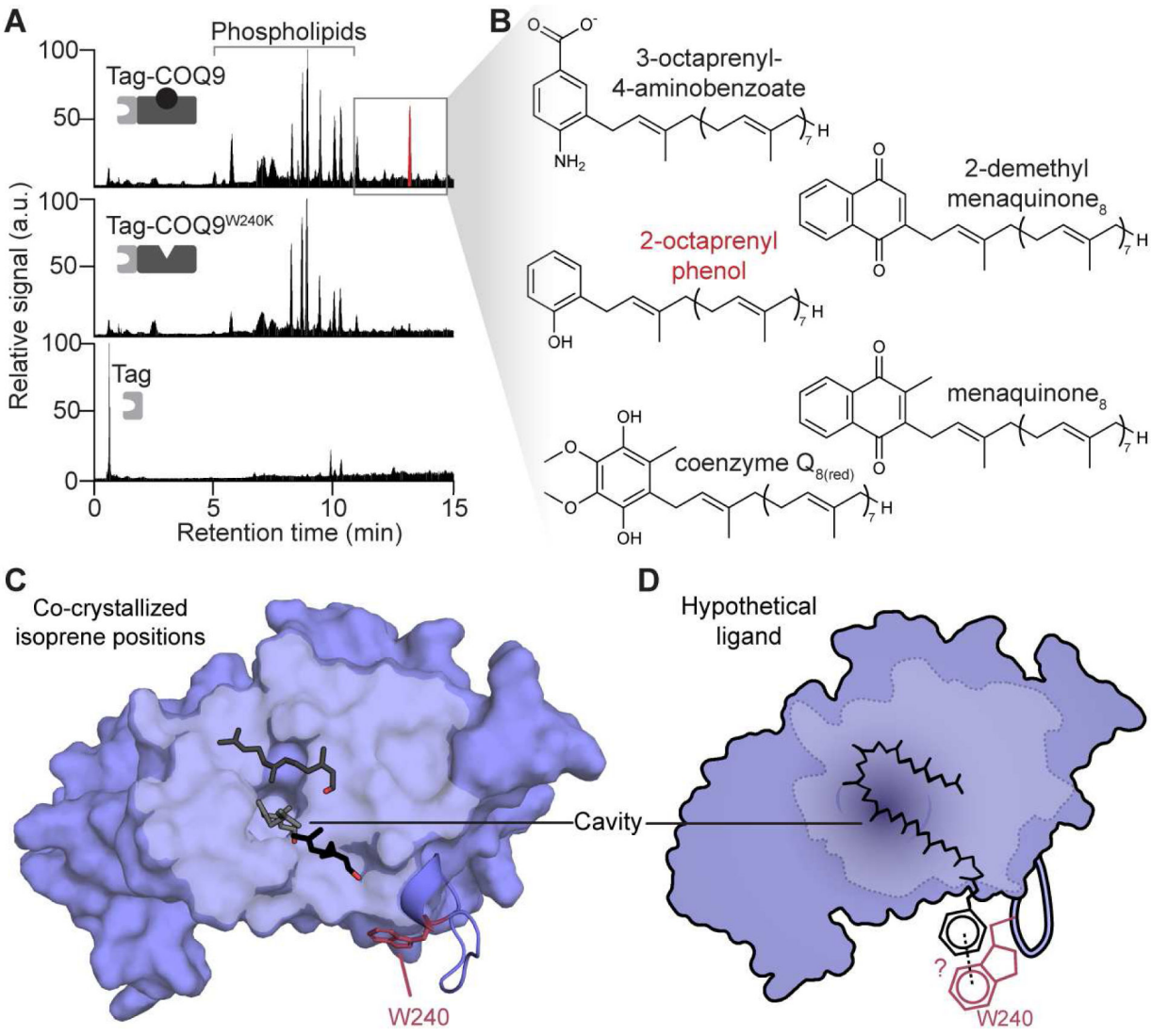


**Figure 1. COQ9 binds aromatic isoprenes.**

(A) LC-MS/MS total ion chromatograms of lipids co-purifying with Tag-COQ9$^{N\Delta 79}$, Tag-COQ9$^{N\Delta 79,\ W240K}$, and Tag expressed in *E. coli* where "Tag" is $His_8$ followed by maltose binding protein.

(B) Chemical structures of identified enriched lipids (fold-change > 4, *p*-value < 0.01) in Tag-COQ9$^{N\Delta 79}$ compared to Tag-COQ9$^{N\Delta 79,\ W240K}$ and Tag. The enriched lipid with the highest intensity signal is highlighted in red.

(C)Representative isoprene positions (stick) observed on a hydrophobic surface and in the cavity of COQ9$^{N\Delta 79,C\Delta 31}$ with W240 in red and the hydrophobic surface in light blue (PDB: 6DEW). Of six isoprenes that co-crystallized in various positions on four of the six COQ9 chains (A,B,D,F) in the unit cell, the three shown are representative of distinct placements and are all mapped to a single COQ9 molecule (chain A).

(D) Model for how an aromatic long-chain isoprene could potentially bind on the surface of COQ9, where the COQ9 cavity is shaded, the hydrophobic surface is outlined, and potential π-π stacking interactions with W240 on α7-α8 loop are highlighted.
See also Figures S1, S2 and Table 1.

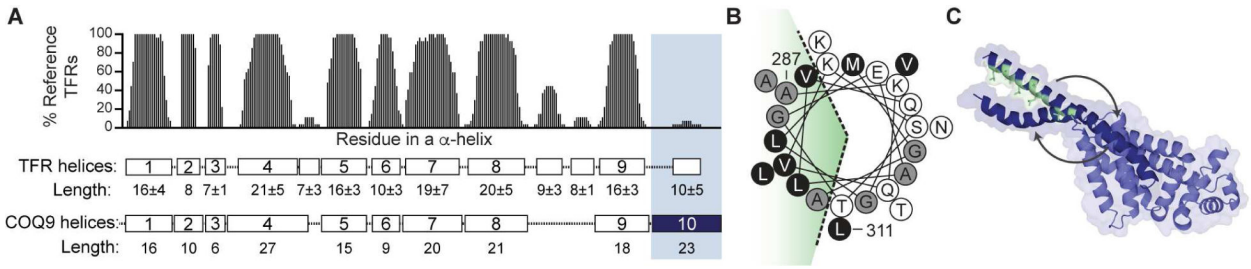


**Figure 2. The 10th α-helix of COQ9 is unique, amphipathic, and flexible.**

(A) Consensus helices of TetR Family Regulators with average length and standard deviation across 27 representative structures (Yu et al., 2010a). COQ9 helices and lengths are mapped below with α10 in dark blue. The presence and length of COQ9's α10 is uncommon among TFRs.

(B) Helical wheel of α10 (A287-L311) with the hydrophobic face highlighted in green, hydrophobic residues in black, A and G in gray, and polar residues in white.

(C) Snapshots of COQ9 with three positions of α10 (dark blue) sampled during CG-MD solution simulations (see Movie S1), where hydrophobic residues are green.

See also Figure S2 and Table 1.

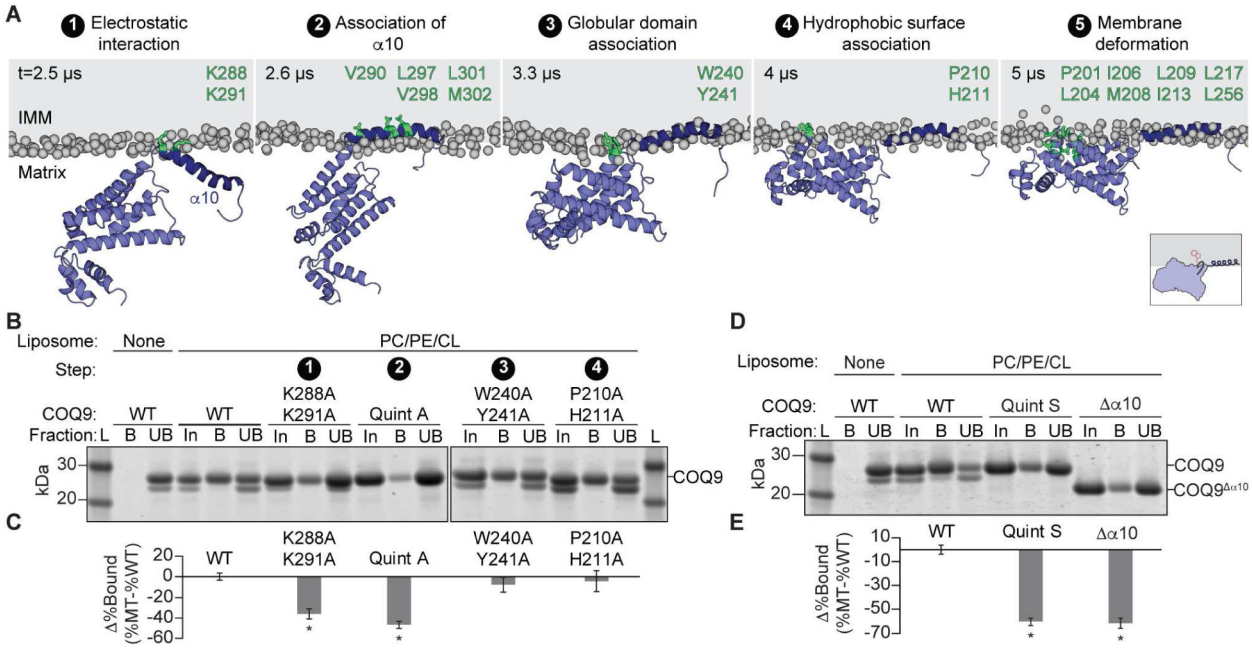


**Figure 3. COQ9 associates with membranes in 5 steps.**

(A) Snapshots representative of the multi-step COQ9 membrane binding mechanism observed in CG-MD simulations (phospholipid head groups in gray and membrane-interacting residues of COQ9 in green; COQ9 model based on PDB: 6AWL).

(B) SDS-PAGE of liposome co-flotation of $COQ9^{N\Delta 79}$ alanine mutants with PC/PE/CL/NBD-PE (68.9/9/22/0.1%) liposomes where L is ladder; In, protein input; B, liposome bound protein; and UB, unbound protein.

(C) Quantification of liposome bound COQ9 alanine mutants (MT) in panel B relative to WT by densitometry ($100\times(B_{MT}/Total_{MT} - B_{WT}/Total_{WT})$ where * indicates a significant ($p$-value < 0.05, n=3) difference from WT binding and error bars represent standard deviation.

(D) SDS-PAGE of liposome co-flotation of COQ9 α10 mutants in PC/PE/CL/NBD-PE (68.9/9/22/0.1%) liposomes where Quint S is V290S,L297S,V298S,L301S,M302S, Δα10 is $COQ9^{N\Delta 79,C\Delta 31}$.

(E) Quantification of liposome bound COQ9 mutants in panel D relative to WT by densitometry ($100\times(B_{MT}/Total_{MT} - B_{WT}/Total_{WT})$) where * indicates a significant ($p$-value < 0.05, n=3) difference from WT binding and error bars represent standard deviation.

**See also** Figure S3.

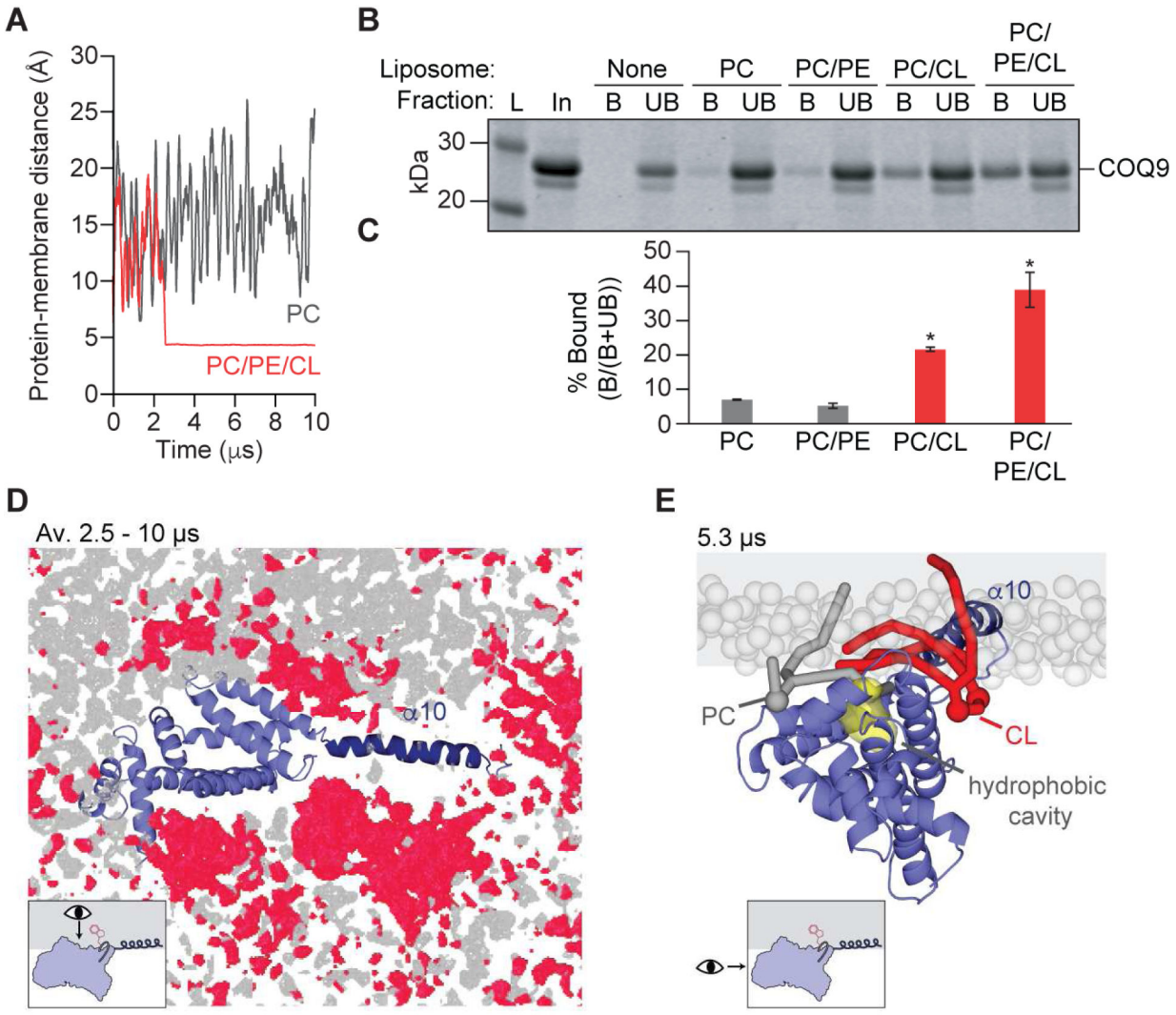


**Figure 4. COQ9 binds and warps cardiolipin-containing membranes.**

(A) Time evolution of the minimum pairwise distance between COQ9 and the membrane (PC or PC/PE/CL) in CG-MD simulations.

(B) SDS-PAGE of liposome co-flotation of $COQ9^{N\Delta 79}$ with PC/NBD-PE (99.9/0.1 molar %), PC/PE/NBD-PE (90.9/9/0.1%), PC/CL/NBD-PE (77.9/22/0.1%), or PC/PE/CL/NBD-PE (68.9/9/22/0.1%) liposomes, as described in Figure 3.

(C) Quantification of liposome bound COQ9 in panel B by densitometry (100×B/Total) where * indicates a significant ($p$-value < 0.05, n=2) difference from PC liposomes and error bars represent standard deviation.

(D) The occupancy of lipid phosphate head groups averaged throughout a 7.5 μs CG-MD simulation during membrane interaction, with phosphate head groups of CL in red and PC/PE in gray, viewed from inside the membrane.

(E) Snapshot from a CG-MD simulation after Step 5 where CL (red) and PC (gray) acyl tails enter the COQ9 hydrophobic cavity (yellow), viewed from the N-terminus of COQ9.

See also Figure S3.

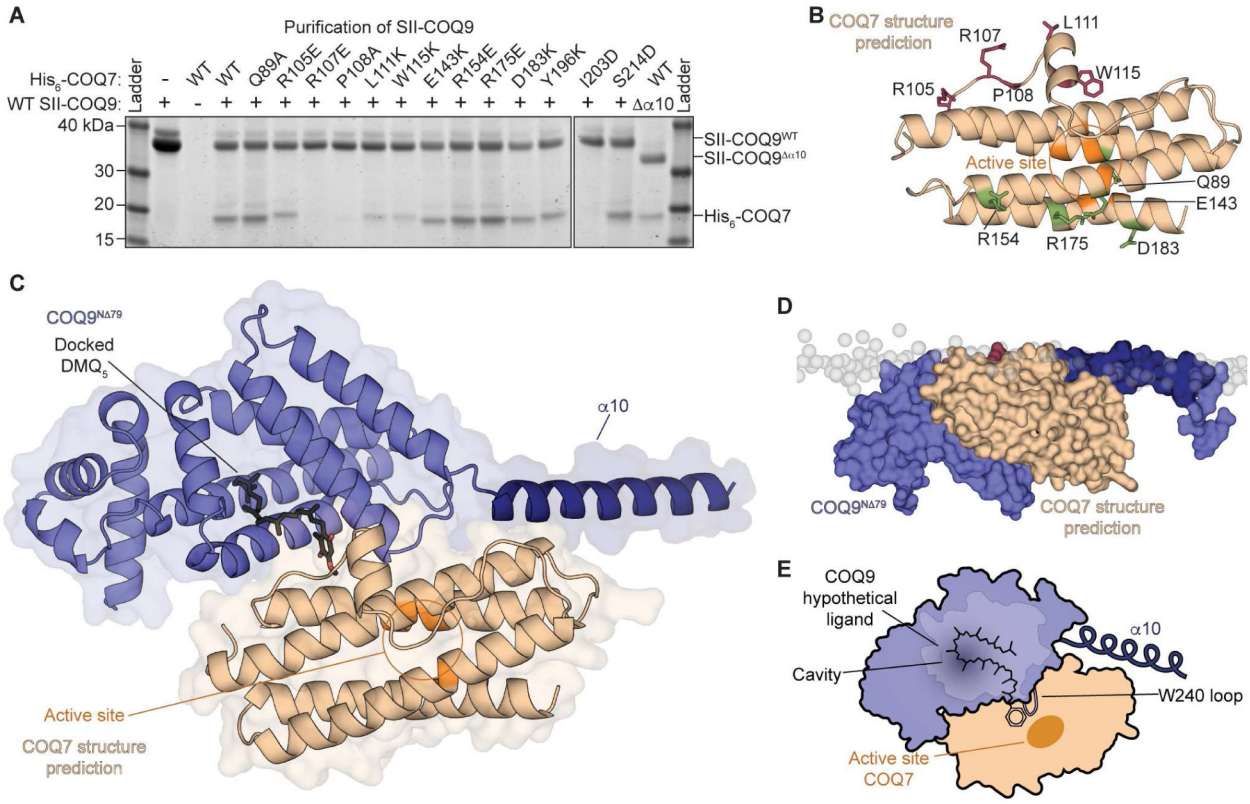


**Figure 5. COQ9 and COQ7 predicted molecular interface suggests substrate presentation.**

(A) SDS-PAGE of $His_6$-$COQ7^{N\Delta 38}$ mutants co-translated with SII-$COQ9^{N\Delta 45}$ or SII-$COQ9^{N\Delta 45,C\Delta 31}$ in cell-free wheat germ extract and purified by the SII-tag on COQ9.

(B) Predicted structure of COQ7 with residues tested in panel (a) labeled, where mutants to residues that affect COQ9 binding are in red, those that do not are in green, and the putative active site residues are highlighted in orange.

(C) Predicted model of the COQ9-COQ7 complex with $DMQ_5$ docked to COQ9 overlaid.

(D) Predicted COQ9-COQ7 complex with the IMM overlaid.

(E) Model for how COQ9 could potentially present substrate to COQ7, viewed from inside the membrane.

See also Figures S4 and S5.

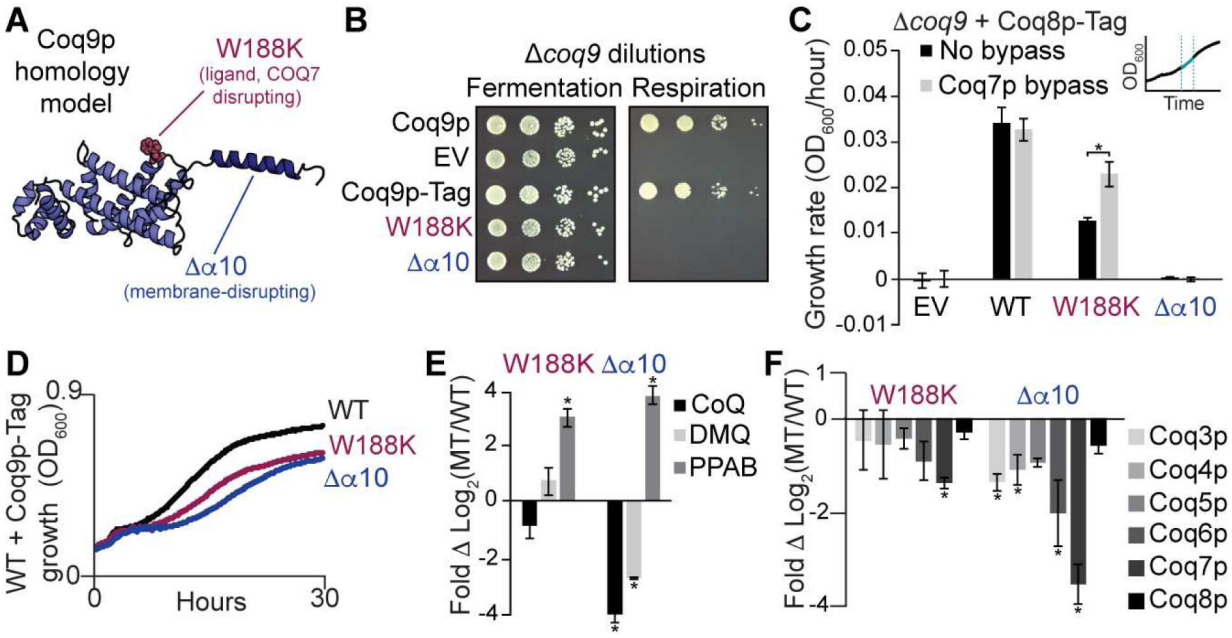


**Figure 6. Coq9p protein-, lipid- and membrane-disrupting mutants perturb endogenous CoQ biosynthesis.**

(A) Homology model of *S. cerevisiae* Coq9p with W188K (lipid- and COQ7-disrupting mutant that is analogous to W240K in human) in red and Δα10 ($Coq9p^{C\Delta 28}$, membrane-disrupting mutant) in blue.

(B) Genetic complementation of Δ*coq9 S. cerevisiae* in fermentation (CoQ-independent) and respiration (CoQ-dependent) conditions where EV is empty vector and mutants have a C-terminal FLAG tag.

(C) Respiration growth rates ($OD_{600}$/hr, linear slope post-diauxic shift as shown in inset) of Δ*coq9 S. cerevisiae* overexpressing Coq8p-FLAG along with Coq9p-FLAG mutants, and the Coq7p chemical bypass 2,4-dihydroxybenzoate (gray bars) where * indicates a significant difference (*p*-value < 0.05, n=3) and error bars represent standard deviation.

(D) Growth curves of WT *S. cerevisiae* overexpressing Coq9p-FLAG mutants in respiration conditions, plotted as an average of monoclonal transformants (n=3).

(E) Fold changes of CoQ intermediates from monoclonal WT *S. cerevisiae* overexpressing Coq9p-FLAG mutants compared to WT Coq9p-FLAG. PPAB is 3-hexaprenyl-4-aminobenzoate, DMQ is demethoxy CoQ, and * indicates a significant difference (absolute value $\Delta Log_2 > 1$, *p*-value < 0.05, n=3) from WT Coq9p-FLAG.

(F) Fold changes of complex Q protein levels from monoclonal WT *S. cerevisiae* overexpressing Coq9p-FLAG mutants compared to WT Coq9p-FLAG, where * indicates a significant change (absolute value $\Delta Log_2 > 1$, *p*-value < 0.05, n=3) from WT Coq9p-FLAG. See also Figures S6 and S7.

## KEY RESOURCES TABLE

| REAGENT or RESOURCE | SOURCE | IDENTIFIER |
|---|---|---|
| Antibodies | | |
| Monoclonal ANTI-FLAG® M2 antibody produced in mouse | Sigma-Aldrich | F1804 RRID:AB_262044 |
| RDye® 800CW Goat anti-Mouse IgG (H + L) | VWR | 926-32210 RRID:AB_621842 |
| Anti-FLAG® M2 Magnetic Beads | Sigma-Aldrich | M8823 RRID:AB_2637089 |
| Bacterial and Virus Strains | | |
| *E. coli* strain BL21-CodonPlus(DE3)-RIPL | Agilent | Cat# 230280 |
| *E. coli* strain DH5α | NEB | Cat# C2987I |
| Chemicals, Peptides, and Recombinant Proteins | | |
| Coenzyme $Q_{10}$; $CoQ_{10}$ | Sigma Aldrich | Cat#C9538 |
| Phosphatidylcholine (mixed species, egg) | Avanti Polar Lipids | Cat#84001C |
| 18:1 NBD-Phosphatidylethanolamine | Avanti Polar Lipids | Cat#810145C |
| 18:1 Phosphatidylethanolamine (“DOPE”) | Avanti Polar Lipids | Cat#850725C |
| 18:1 Cardiolipin | Avanti Polar Lipids | Cat#710335C |
| 2,4-dihydroxybenzoic acid | Sigma-Adrich | D109401 |
| 3,4-dihydroxybenzoic acid | Sigma-Adrich | P5630 |
| Vanillic acid | Sigma-Adrich | H36001 |
| 4-hydroxy-2-methylbenzoic acid | Sigma-Adrich | 653160 |
| FLAG peptide | Sigma-Aldrich | F3290 |
| TALON resin | Clontech | 635503 |
| StrepTactin Sepharose High Performance Resin | GE | 28935599 |
| Sypro Orange (5000X) | Thermo Fisher | S-6650 |
| SP6 RNA polymerase | Promega | P1085 |
| RNasIn | Promega | N2111 |
| Creatine kinase | Roche | 10736988001 |
| Geranylgeraniol | Sigma | G3278 |
| Critical Commercial Assays | | |
| Sypro™ Ruby Protein Gel Stain | Thermo Fischer | S12000 |
| Deposited Data | | |
| $COQ9^{N\Delta 79}$ P21 | Protein Data Bank | PDB ID: 6AWL |

| REAGENT or RESOURCE | SOURCE | IDENTIFIER |
|---|---|---|
| $COQ9^{N\Delta79,\ C\Delta31}$ GG | Protein Data Bank | PDB ID: 6DEW |
| Thermo Fisher Scientifc *.raw Files | Chorus Project | Proteomics ID: 1532 Lipidomics ID: 1533 |
| Image data | Mendeley Data | http://dx.doi.org/10.17632/63ztbyhx5h.1 |
| Experimental Models: Organisms/Strains | | |
| *S. cerevisiae* WT BY4742 alpha haploid his3Δ1 leu2Δ0 lys2Δ0 ura3Δ0 | GE Dharmacon | Cat#YSC1049 |
| *S. cerevisiae Δcoq9* BY4742 alpha haploid his3Δ1 leu2Δ0 lys2Δ0 ura3Δ0 | Thermo collection #YSC1054 | Thermo YSC6272-201920350 |
| Wheat germ cell free extract | CellFree Sciences | WEPRO2240 |
| Oligonucleotides | | |
| See primer table | | |
| Recombinant DNA | | |
| Coq9p-LDLE-FLAG p416GPD | Guo et al. 2017 | N/A |
| Coq9p-LDLE-FLAG W188K p416GPD | This work | N/A |
| Coq9p G232 Stop (Δα10) p416GPD | This work | N/A |
| Coq9p G232-8XGlycine-FLAG (Δα10) p416GPD | This work | N/A |
| Coq8p-LDLE-FLAG p413GPD | This work | N/A |
| $His_8$-MBP-tev-$COQ9^{N\Delta79}$ HR5043-79-318-MBP3.11 | Lohman et al. 2014 | N/A |
| $His_8$-MBP-tev-$COQ9^{N\Delta79}$ W240K HR5043-79-318-MBP3.11 | Lohman et al. 2014 | N/A |
| $His_8$-MBP-tev-$COQ9^{N\Delta79}$ K288A,K291A HR5043-79-318-MBP3.11 | This work | N/A |
| $His_8$-MBP-tev-$COQ9^{N\Delta79}$ W240A,Y241A HR5043-79-318-MBP3.11 | This work | N/A |
| $His_8$-MBP-tev-$COQ9^{N\Delta79}$ P210A,H211A HR5043-79-318-MBP3.11 | This work | N/A |
| $His_8$-MBP-tev-$COQ9^{N\Delta79}$ V290A,L297A,V298A, L301A,M301A (QuintA) HR5043-79-318-MBP3.11 | This work | N/A |
| $His_8$-MBP-tev-$COQ9^{N\Delta79}$ V290S,L297S,V298S, L301S,M301S (QuintS) HR5043-79-318-MBP3.11 | This work | N/A |
| $His_8$-MBP-tev-$COQ9^{N\Delta79}$ A287 Stop (Δα10) HR5043-79-318-MBP3.11 | This work | N/A |
| $His_6$-MBP pET28 | Addgene | 69929 |
| $His_6$-$COQ7^{N\Delta38}$ pEU | Lohman et al. 2014 | N/A |
| $His_6$-$COQ7^{N\Delta38}$ W115K pEU | This work | N/A |

| REAGENT or RESOURCE | SOURCE | IDENTIFIER |
|---|---|---|
| $His_6$-COQ7 $^{N\Delta 38}$ R105E pEU | This work | N/A |
| $His_6$-COQ7 $^{N\Delta 38}$ R107E pEU | This work | N/A |
| $His_6$-COQ7 $^{N\Delta 38}$ R154E pEU | This work | N/A |
| $His_6$-COQ7 $^{N\Delta 38}$ Q89A pEU | This work | N/A |
| $His_6$-COQ7 $^{N\Delta 38}$ E143K pEU | This work | N/A |
| $His_6$-COQ7 $^{N\Delta 38}$ R175E pEU | This work | N/A |
| $His_6$-COQ7 $^{N\Delta 38}$ D183K pEU | This work | N/A |
| $His_6$-COQ7 $^{N\Delta 38}$ I203D pEU | This work | N/A |
| $His_6$-COQ7 $^{N\Delta 38}$ S214D pEU | This work | N/A |
| $His_6$-COQ7 $^{N\Delta 38}$ Y196K pEU | This work | N/A |
| $His_6$-COQ7 $^{N\Delta 38}$ P108A pEU | This work | N/A |
| $His_6$-COQ7 $^{N\Delta 38}$ L111K pEU | This work | N/A |
| $His_6$-COQ7 $^{N\Delta 38}$ E178K pEU | This work | N/A |
| SII-COQ9 $^{N\Delta 45}$ pEU | Lohman et al. 2014 | N/A |
| SII-COQ9 $^{N\Delta 45}$ A287 Stop (Δα10) pEU | This work | N/A |
| Coq8p p416 | Reidenbach et al. 2018 | N/A |
| Yeast ORF KES1 (YPL145C) | Dharmacon | YSC3867-202330173 |
| Human ORF VCADL | DNASU | 28492 |
| Yeast ORF OPI1 (YHL020C) | Dharmacon | YSC3867-202327190 |
| Software and Algorithms | | |
| Image Studio v5.2 software | LI-COR | https://www.licor.com/bio/products/software/image_studio/?gclid=CjwKEAjw_PfGBRDW_sutqMbQsmMSJAAMpUapnCbeDQSTBAWjOLZv7FuyOMGKZxDTzL0XUOTKhqx6_RoCFMrw_wcB |
| MaxQuant | Max Planck Institute of Biochemistry | Version 1.5.0.25 |
| TraceFinder v4.0 | Thermo Fisher | https://www.thermofisher.com/order/catalog/product/OPTON-30491 |
| Compound Discoverer 2.0 | Thermo Fisher | https://www.thermofisher.com/order/catalog/product/OPTON-30833?SID=srch-srp-OPTON-30833 |
| LipiDex | Hutchins 2018 | |
| MSConvertGUI | ProteoWizard, Dr. Parag Mallick, Stanford University | http://proteowizard.sourceforge.net/tools.shtml |
| Protein thermal shift | Thermo Fisher | 4466038 |
| XDS, XSCALE | Kabsch 2010 | http://xds.mpimf-heidelberg.mpg.de/ |

| REAGENT or RESOURCE | SOURCE | IDENTIFIER |
|---|---|---|
| Phenix suite | Adams et al. 2010 | https://www.phenix-online.org |
| Phaser | McCoy et al. 2007 | http://www.phaser.cimr.cam.ac.uk/index.php/Phaser_Crystallographic_Software |
| Phenix.refine | Afonine et al. 2012 | https://www.phenix-online.org/documentation/reference/refinement.html |
| Coot | Emsley et al. 2010 | https://www2.mrc-lmb.cam.ac.uk/personal/pemsley/coot/ |
| The PyMOL Molecular Graphics System, v2.0 | Schrödinger LLC | ghttps://pymol.org/2/ |
| VMD v1.9 | Humphrey et al. 1996 | https://www.ks.uiuc.edu/Research/vmd/ |
| GROMACS v5.1.2 | Abraham et al. 2015 | http://manual.gromacs.org/documentation/ |
| ICM-Pro Molecular modeling software | Molsoft LLC Abagyan et al. 1994 | http://www.molsoft.com/icm_pro.html |
| SWISS-MODEL Server | Schwede et al. 2003 | https://swissmodel.expasy.org/ |
| Modeller v9.11 | Andrej Sali, UCSF Webb and Sali 2017 | https://salilab.org/modeller/ |
| ZDock Server | Pierce et al. 2014 | http://zdock.umassmed.edu/ |
| Other | | |
| Fusion Orbitrap Tribrid | Thermo Fisher | IQLAAEGAAPFADBMBCX |
| Cytation 3 | BioTek | N/A |
| Licor CLX | Licor | N/A |
| StrataX polymeric reverse phase spe cartridges | Phenomenex | 8B-S100-AAK |
| Q Exactive HF | Thermo Fisher | IQLAAEGAAPFALGMBFZ |
| Vanquish Binary Pump | Thermo Fisher | VH-P10-A |
| Vanquish Split Sampler | Thermo Fisher | VF-A10-A |
| Vanquish Column Compartment | Thermo Fisher | VH-C10-A |
| ACQUITY UPLC CSH C18 Column | Waters | 186005297 |
| nanoACQUITY UPLC binary pumps | Waters | 186016007 |
| nanoAcquity UPLC autosampler | Waters | 186016002 |
| BEH 1.7 μm C18 columns | Waters | 186003569 |
| Flexible fused silica capillary tubing 75μm ID | Molex | TSP075375 |
| QuantStudio 6 Flex Real-Time PCR System | Thermo Fisher | 4485697 |
| Mini-extruder set (for liposome extrusion) | Avanti Polar Lipids | Cat#610000 |
| Sorvall MX 120 Plus Micro-ultrafuge | Thermo Fisher | 50135645 |
| HiLoad 16/600 Superdex 75 pg | GE Healthcare | 28989333 |
| Mosquito HTS | TTP Labtech | https://www.ttplabtech.com |

| REAGENT or RESOURCE | SOURCE | IDENTIFIER |
|---|---|---|
| UVEX-P | JanSCI | http://janscientific.com |
| Eiger 9M, Eiger 16M | DECTRIS Ltd | https://www.dectris.com/products/eiger/eiger-x-for-synchrotron |

**Table 1:**
**Data collection and refinement statistics.**

Statistics for the highest-resolution shell are shown in parentheses.

| | **COQ9$^{N\Delta 79}$ P21 (PDB ID 6AWL)** | **COQ9$^{N\Delta 79, C\Delta 31}$ GG (PDB ID 6DEW)** |
|---|---|---|
| Wavelength | 1.033 | 1.127 |
| Resolution range | 48.69 – 2.0 (2.071 – 2.0) | 48.0 – 2.0 (2.071 – 2.0) |
| Space group | P 1 21 1 | C 2 2 21 |
| Unit cell | 38.11 97.39 63.65 90 95.4 90 | 116.45 222.78 130.78 90 90 90 |
| Total reflections | 159831 (15769) | 1545884 (159984) |
| Unique reflections | 31219 (3066) | 114146 (11326) |
| Multiplicity | 5.1 (5.1) | 13.5 (14.1) |
| Completeness (%) | 99.90 (100.00) | 99.68 (99.87) |
| Mean I/sigma(I) | 12.38 (1.25) | 15.48 (1.51) |
| Wilson B-factor | 36.31 | 37.83 |
| R-merge | 0.09055 (1.355) | 0.1274 (1.759) |
| R-meas | 0.101 (1.51) | 0.1325 (1.824) |
| R-pim | 0.04409 (0.658) | 0.03598 (0.4802) |
| CC1/2 | 0.998 (0.48) | 0.998 (0.622) |
| CC* | 1 (0.805) | 1 (0.876) |
| Reflections used in refinement | 31212 (3066) | 114124 (11326) |
| Reflections used for R-free | 2000 (197) | 2045 (197) |
| R-work | 0.1974 (0.3016) | 0.1692 (0.2626) |
| R-free | 0.2454 (0.3183) | 0.2094 (0.3055) |
| CC(work) | 0.957 (0.710) | 0.967 (0.817) |
| CC(free) | 0.962 (0.679) | 0.947 (0.730) |
| Number of non-hydrogen atoms | 3564 | 9744 |
| macromolecules | 3313 | 9183 |
| ligands | 46 | 106 |
| solvent | 205 | 455 |
| Protein residues | 409 | 1138 |
| RMS(bonds) | 0.003 | 0.019 |
| RMS(angles) | 0.64 | 1.59 |
| Ramachandran favored (%) | 97.52 | 97.69 |
| Ramachandran allowed (%) | 1.98 | 2.13 |
| Ramachandran outliers (%) | 0.50 | 0.18 |
| Rotamer outliers (%) | 1.12 | 0.51 |
| Clashscore | 4.21 | 4.09 |
| Average B-factor | 43.21 | 52.11 |
| macromolecules | 42.82 | 51.61 |
| ligands | 63.56 | 102.08 |

| | **COQ9$^{N\Delta 79}$ P21 (PDB ID 6AWL)** | **COQ9$^{N\Delta 79,\ C\Delta 31}$ GG (PDB ID 6DEW)** |
|---|---|---|
| solvent | 44.83 | 50.57 |
| Number of TLS groups | | 36 |